Introducing aerosol-cloud interactions in the ECMWF model reveals new constraints on aerosol representation

Paolo Andreozzi[1, 2, 3, 4], Mark D. Fielding[1], Robin J. Hogan[1], Richard M. Forbes[1], Adrian A. Hill[1], Samuel Rémy[5], Birger Bohn[3], and Ulrich Löhnert[3,4]

[1]European Centre for Medium-Range Weather Forecasts, Bonn (Germany) and Reading (United Kingdom)
[2]Deutscher Wetterdienst, Offenbach (Germany)
[3]Forschungszentrum Jülich, Jülich (Germany)
[4]University of Cologne, Cologne (Germany)
[5]HYGEOS, Lille (France)

Correspondence: Paolo Andreozzi (paolo.andreozzi@ecmwf.int)

Abstract. Realistic number concentrations of aerosol cloud condensation nuclei (CCNcloud droplet number concentrations (N_d) are critical to simulate for simulating the Earth's atmosphere radiative budget. However, CCN concentrations are very uncertain, which critically limits our capacity to precisely predict climate change. This is partly because radiative budget, yet remain challenging to represent in global models. One reason is that aerosol optical depth (AOD)observations, traditionally used for validation of and assimilationinto aerosol models, weakly constrain number concentrations , commonly used for aerosol validation and assimilation, only weakly constrains aerosol number concentrations relevant for cloud formation. We introduce a physically informed representation of aerosol-cloud interactions (ACI) in the European Centre for Medium-Range Weather Forecasts (ECMWF) into the ECMWF Integrated Forecasting System (IFS)to simulate the activation of aerosols into cloud droplets driven by aerosol concentrations from , restricted to aerosol activation and the first indirect effect, and use it as a diagnostic tool to relate aerosol properties to cloud observations in the Copernicus Atmosphere Monitoring System (CAMS), using offline computations from a parcel model. Then, we use an 18-year-long series of MODIS cloud droplet number concentrations (. Using 18 years of MODIS N_d) retrievalsto tune retrievals, we optimise aerosol size distributions and simulated number concentrations. Finally, we validate the system using AOD observations , all-sky broadband SW fluxes, Angstrom exponentand size spectrafrom satellite and AERONET. We found that CAMS aerosols allows simulating validate results using independent observations of AOD, Angstrom exponent, size spectra, and top-of-atmosphere shortwave fluxes. After optimisation, CAMS aerosols produce overall realistic $N_d$values, but these are systematically overestimated over most of , but exhibit regional biases: overestimation over sub-Saharan Africa and underestimated at latitudes higher than 60°N and 45°S. While the first bias hints at issues underestimation at high latitudes. The African bias is consistent with carbonaceous aerosols from African wildfires , emissions from wildfires and can be partially mitigated through optimisation, while the high-latitude bias originates from too efficient is likely linked to excessive aerosol scavenging in mixed-phase clouds . We finally show that addressing this last issue dramatically improves simulated clouds and cannot be resolved by size adjustments alone. We show that introducing phase-dependent aerosol scavenging substantially improves all-sky shortwave fluxes over the Southern Ocean . This study showcases that representing compared to the ACI implementation in the standard CAMS system. This highlights a direct link between radiative biases and aerosol wet removal processes. Representing ACI in a weather model is a powerful diagnostic tool to improve aerosol representations and processes , potentially informing also applications in climate modelsenables N_d to constrain aerosol processes globally, revealing limitations in how ageing, vertical transport and wet removal are represented, as these processes are only weakly constrained by standard AOD evaluation.

1 Introduction

The number concentration of abundance of aerosols that act as cloud condensation nuclei (CCN) is essential for the simulation of realistic liquid- and mixed-phase clouds radiative properties in weather and climate models. The pathway by which the abundance of available aerosol CCNs determines the number concentration of droplets a primary control on cloud droplet number concentrations (N_d) , and in turn , during cloud formation; N_d in turn determines the cloud droplet effective radius (r_e)is generally . Anthropogenic or natural changes in aerosols can thereby modify N_d and r_e, altering the cloud albedo. This

is referred to as the albedo (or Twomey) effect (Twomey, 1977, 1991) . This is and is related to the first and best understood of a cascade of aerosol indirect effects (Bellouin et al., 2020; Gordon et al., 2023) on the particle size distribution (PSD)of cloud droplets, with repercussions , with consequences on the cloud life cycle, macrophysics, and precipitation (Albrecht, 1989; Pincus and Baker, 1994). Such indirect effects are included under the umbrella-term of aerosol-cloud interactions (ACI). Due to the macroscopic role of clouds in the regulation of the Earth's energy budget, quite complex aerosol-cloud interactions (ACI) have been for ACI are considered necessary in global climate models (Menon et al., 2002; Stier et al., 2005; Penner et al., 2006; Bellouin et al., 2011; Mulcahy et al., 2018)to correctly capture the radiative response to anthropogenic aerosol emissions (Menon et al., 2002; Stier et al., 2005; Penner et al., 2006; Bellouin et al., 2011; Seinfeld et al., 2016; Mulcahy et al., 2018; Wang et al., 2021). However, such representations are still fraught with uncertainties, severely limiting the ability of models to precisely predict climate change due to anthropogenic emissions (Szopa et al., 2023).

Activation of CCN into droplets is described by the Köhler theory (e.g. Pruppacher and Klett, 2010) for heterogeneous nucleation of cloud droplets. The efficiency of CCN in supporting droplet nucleation is notably controlled both by their solubility in water, and the amount of surface available for binding with water molecules. A popular way of describing CCN activation is in the form of the κ-Köhler theory (Petters and Kreidenweis, 2007), where aerosol chemical properties are condensed into a single hygroscopicity parameter κ (Quaas and Gryspeerdt, 2022). Rothenberg and Wang (2016) used this framework in the implementation of an adiabatic parcel lifting model to accurately simulate the maximum supersaturation reached during the ascent of an air parcel . This allows the model to also Since the early formulations by Twomey in the late 1950s, activation models have been produced that can accurately solve the equations derived by the κ-Köhler theory for the air parcel lifting condensation problem (see Ghan et al. (2011) for a detailed review). In addition, climate models deployed fast physical parametrisations and lookup tables that have proven to perform satisfactorily compared to the full numerical models (Ghan et al., 2011).

Some numerical parametrisations can also represent activation of heterogenous aerosol mixtures and kinetic limitations of the activation process (Nenes et al., 2001; Ghan et al., 2011). These are needed to capture the effect of large sea salt particles to prevent on suppressing activation of available sulfate (SO_4^{2-}) aerosols (Fossum et al., 2020). It is, however, unclear what relevance this effect has for realistic aerosol populations and scenarios (Fossum et al., 2020). The relevance of this effect remains however unclear in actual atmospheric conditions, e.g. in terms of regulation of global energy budgets or on the the regulation of the global energy budget or aerosol speciation itself, which could be clarified by more accurate representation of aerosol-cloud interactions explored with more accurate representations of ACI in global models.

In the realm of global numerical weather prediction (NWP), models typically represent aerosol concentrations diagnostically using climatologies (e.g. Tegen et al., 1997; Bozzo et al., 2020). Such simplified descriptions allow beneficial the average aerosol-radiation interaction to be caught while avoiding to resort to computationally costly simulations using prognostic aerosol and chemical tracers, where they are advected and let interacting fully with other components of the system. Within such simplified descriptions, aerosol-cloud interactions are typically neglected. A previous captured while avoiding the computational cost of prognostic aerosol scheme simulations with advection and interaction of tracers. A study by Mulcahy et al. (2014) showed that representing the indirect effect with prognostic aerosol fields has including indirect effects of prognostic aerosols has a widespread and potentially beneficial impact on the radiative budget of an NWP model. Ahlgrimm

et al. (2018) showed that model biases in TOA shortwave (SW) radiative fluxes are dominated by errors in the cloud macrophysics (cloud cover, water phase and content, sub-grid heterogeneity) and but also significantly affected by deficiencies in the cloud microphysics, poor N_d representation and, in turn, r_e values. Global NWP models are also indicating that those biases might be reduced by representing ACI. Furthermore, global NWP models have already started moving toward more complex two-moment cloud schemes (Field et al., 2023), where both water content and droplet number concentrations are prognostic variables; this direction implies an even higher importance of realistic CCN values for the cloud microphysics. Despite this, the uncertainty of the physical processes involved in ACI and the difficulties in providing enough observational constraints (Rasch and Carslaw, 2022) have for a long time constituted a major challenge. However, the evolution of such systems towards higher integration of applications, from air quality (Baklanov et al., 2017) to weather forecasts and climate simulations (Palmer et al., 2008) unlocks unprecedented weather and climate forecasting systems towards more comprehensive Earth system representations, including air quality (Baklanov et al., 2017; Palmer et al., 2008), opens new opportunities for the validation of processes and representations. In addition to this, NWP models are thoroughly tested and monitored every day with a wide range of observations, which makes them an important testbed test bed for ACI schemes. This offers the potential to refine these schemes in such a way that can also inform climate models.

The Integrated Forecasting System (IFS) used at the European Centre for Medium-Range Weather Forecasts (ECMWF) is a ECMWF) is an NWP model used to perform operational global meteorological analysis and forecasts on the medium- (10 days), extended- sub-seasonal (42 days) and long- seasonal (4 months) range. The IFS also supports a configuration an atmospheric-chemistry configuration denoted as IFS-COMPO (Flemming et al., 2015), with online chemistry and aerosol tracers, that is developed and maintained within on behalf of the Copernicus Atmosphere Monitoring Service (CAMS)and denoted as IFS-COMPO (Flemming et al., 2015). In the IFS-COMPO / CAMS configuration, a bin bulk mass "bulk-bin" prognostic representation of aerosols is used (Rémy et al., 2022), but their feedback into onto meteorological fields is only mediated by the direct radiative effect. The IFS currently diagnoses N_d values for the calculation of r_e in liquid clouds using a wind-dependent parametrization that changes parametrisation that differs between land and sea, but that has no dependence in on either climatological or prognostic aerosols (ECMWF, 2024b). Similarly, the IFS uses fixed N_d values over land and sea for the calculation of cloud-to-rain water auto-conversion rates. Similar simplified descriptions have been typical for NWP, but the increasing resolution of operational forecasts naturally leads to the demand for more realistic representations of aerosol-cloud interactions (Wilkinson et al., 2013).

Improving the representation of aerosol-cloud-interactions (ACI) ACI in the IFS is therefore a strategic aim a potential area of development at ECMWF, both for CAMS and NWP forecasts. ACI must also reflect the quality of the information provided by aerosol fields, either in a prognostic or climatological representation, the latter being used for forecasts on the medium-range (up to 10 days) and longer timescales (months). A major goal of this study was to associate recent study by Block et al. (2024) showed that the aerosols from the CAMS reanalysis (CAMSRA) can provide CCN diagnostics for validation against in-situ observations, but also revealed systematic errors hinting at underlying model issues. This illustrates the need for improved model aerosol descriptions to induce as realistic as possible values of droplet number concentrations (global CCN concentrations and N_d) values in liquid cloudsto aerosol mass mixing ratios (MMR) in the model. In order to , which

constitutes the main goal of this study. To achieve this, we designed a method to efficiently constrain simulated number concentrations from prognostic aerosol using an 18-years long 18-year dataset of MODIS N_d retrievals . spanning 2003–2020. Consistently with the satellite retrievals, throughout this work we treat N_d diagnostically; we do not explicitly distinguish between activation-stage and in-cloud N_d, in line with the diagnostic nature of the modelling framework and the assumption of vertically uniform N_d embedded in satellite retrievals. The general concept behind our approach has similarities to that adopted by McCoy et al. (2018), who used near-surface daily-mean aerosols mass concentrations of sulfate and sea salt aerosol from MERRA2 reanalyses to predict MODIS N_d retrievals. In contrast, our method introduces several new aspects: firstly, we simulate the near real-time activation of aerosol particles activation of time-resolved aerosol fields into cloud droplets using an offline version of the aerosol activation scheme. Secondly, instead of using a fixed level above the surface we systematically collocate aerosols and clouds to accurately assess characterise the atmospheric composition at cloud level. Thirdly, instead of optimizing optimising mass-to-number conversion coefficients, we optimize optimise the underlying particle size distribution (PSDdistributions (PSDs) of the bulk aerosols . By using and evaluate their physical consistency against independent observations of aerosol optical properties. Using this approach, we are also in the position to can also interpret the results of the optimization optimisation in terms of aerosol representation and assess evaluate consistency with other represented processes, such as theirdirect radiative effect. Finally, results of the optimization procedure could be tested with simulations using the IFS the ACI scheme resulting from the optimisation procedure is tested in IFS simulations with prognostic aerosols.

The core question of this study is whether N_d observations can globally constrain aerosol number representations in a system used for operational atmospheric composition analyses and forecasts, and which deficiencies in aerosol processe such constraints reveal. This work has the following structure: Section 2 illustrates describes the mass-bulk representation of aerosols in the IFS and clarifies the impact of aerosol PSD definitions on particle number concentrations and aerosol optical depth; Section 3 describes the observational data used for this study; Section 4 describes the methodology of the study, including the aerosol activation scheme of the IFS, the datasets of observations and the model data; Section 5 presents and discusses the results of the optimization optimisation procedure; Section 6 describes the impact of a modified wet-scavenging scheme for mixed-phase clouds on the simulated first indirect effect of aerosols. In Section 8 we provide a summary of findings, together with conclusions and possible future outlooksSection 7 discusses the results, and Section 8 provides a summary and outlook.

2 Aerosol representationsin the IFS

The IFS-COMPO Cycle CY49R1.0 is equipped with the of the IFS-COMPO uses the 'IFS-AER' single moment aerosol scheme (Rémy et al., 2022), where mass concentrations for each aerosol species are prognostic tracers. Optionally, the model can use a model-derived with a bulk mass representation of aerosol tracers. Alternatively, the IFS can also use a reanalysis-derived climatology of aerosols (Bozzo et al., 2020), in which case, the IFS-AER scheme is switched off. Currently, the IFS only includes the direct radiative effect of aerosols. Meteorology impacts which is the default for operational NWP. Meteorology affects aerosol optical properties via hygroscopic growth and, in a prognostic configuration, their production, transport and removal. However, feedbacks of aerosol-related processes aerosol feedbacks on meteorological fields are only mediated by influence of aerosol-radiation interactions the impact of the direct radiative impact of aerosols on heating rates(semi-direct effect of aerosols). The IFS .

IFS-COMPO represents 8 types of aerosols in a bulk representation. These are listed , that are reported in Table 1. Among these, Some species like sea salt (SS) and mineral dust (DU) aerosol species consist of multiple partitions of a broader particle size range, configuring a so-called mixed binned-bulk aerosol scheme. All aerosols in the IFS interact with radiation by bulk optical properties obtained via Mie computations. To this purpose, they are represented by lognormal multimodal PSD, which is referred to as a 'bulk-bin' representation. Bulk optical properties for each species are computed using Mie calculations with a prescribed log-normal number PSD, with median radius r_{med} and shape parameter or (geometric standard deviation) σ (ECMWF, 2024a). The normalized PSD Throughout this study, aerosol PSDs refer to dry aerosol, and the normalized distribution $n(r)$ is given by: defined as

$$n(r) = \sum_{i=1}^{N} a_i n_i(r) = \sum_{i=1}^{N} \frac{a_i}{\sqrt{2\pi}\, r\, \ln\sigma_i}\, e^{-\frac{\ln^2(r/r_{\text{med},i})}{2\ln^2\sigma_i}} \tag{1}$$

where N_0 is the total number density of particles, for multimodal species (sea salt and mineral dust): where i indicates each mode of the distribution and α_i a_i are weight coefficients such that $\sum \alpha_i = 1$. Definitions of aerosol tracers and are reported in Table 1. $\sum a_i = 1$.

Hydrophilic species undergo hygroscopic growth by water uptake- , described as a function of relative humidity. This is used to determine , which affects refractive index and optical properties used by the radiation schemeparticle size due to the mixing with water, which are relevant to transport processes and radiative transfer calculations. Hydrophilic species are also removed undergo a removal process when precipitation occurs, with a fixed mass scavenging rate described in ECMWF (2024a) and following Luo et al. (2019). Aerosols in the IFS are represented as

The externally-mixed species. This means that representation of CAMS aerosols has relevant consequences on process descriptions. For example, the optical properties of a mixed population aregiven by superposition principle from , by superposition assumption, given by the sum of its components. The model is not able to fully represent those aging processes where organics or black carbon form clusters with sulfate particles in aqueous phaseMoreover, the model is unable to represent those ageing processes where organic matter (OM), black carbon (BC) or sulfate (SU) particles cluster together to form new particles. While such ageing processes conserve the mass of the involved species considered as separate entities, they also affect

Aerosol type	Size bin limits (sphere radius [μm])	ρ [$\mathrm{g/cm^3}$]	r_{med} [μm]	σ
Sea Salt (SS)		1.183	$0.1, 1.0$	$1.9, 2.0$
bin 1 (SS1)	0.015-0.25			
bin 2 (SS2)	0.25-2.5			
bin 3 (SS3)	2.5-10			
Mineral Dust (DU)†		2.61	$0.05, 0.42, 0.79, 16.2$	$2.2, 1.18, 1.93, 1.53$
bin 1 (DU1)	0.03-0.55			
bin 2 (DU2)	0.55-0.9			
bin 3 (DU3)	0.9-20			
Black carbon (BC, BCH)*	0.005-0.5	1.0	0.0118	2.0
Sulfates (SU)	0.005-20	1.76	0.11	1.6
Organic matter (OM, OMH)*	0.005-20	1.3	0.09	1.6
Secondary Organic matter				
Biogenic (SOB)	0.005-20	1.8	0.09	1.6
Anthropogenic (SOA)	0.005-20	1.8	0.09	1.6
Nitrates (NI)				
Fine (NIF)	0.03-0.9	1.73	0.0355	2.0
Coarse (NIC)†	0.9-20	1.40	$0.199, 1.992$	$1.9, 2.0$
Ammonium (AM)	0.005-20	1.76	0.0355	2.0

Table 1. Aerosol species in IFS-COMPO CY49R1.0, from Rémy et al. (2022) and ECMWF (2024a). ρ is the species density, while r_{med} and σ the geometric mean and standard deviation of the associated log-normal distribution. All species are hydrophilic, except those marked with *, that are represented by a hydrophilic and a hydrophobic tracer, and the letter H is used to indicate the hydrophilic tracer. Hydrophobic tracers and those marked with † are not used for CCN computations. The number ratios (a_i) of the modes for multimodal PSD are: 0.96 and 0.04 for SS and coarse NI, $0.95, 0.020, 0.028, 3.4\,10^{-7}$ for DU. Note that parameters for all species, including sea salt, are here reported at 0% relative humidity.

speciated aerosol mass, they naturally impact the total number, the PSD and the PSD and refractive index of the resulting aged aerosolspecies. To represent aging, the IFS aerosol scheme converts organic matter (OM) ageing, the IFS-COMPO converts OM and BC from the hydrophobic to the hydrophilic type with an e-folding timescale that can be either prescribed or depending on local chemical composition. In either case, aging does not impact any other chemical or aerosol species, or the refractive index of the aged aerosol. Compared to the hydrophobic type, hydrophilic OM has hygroscopic growthand the refractive index is adjusted to describe the water-aerosol mixture; hydrophilic black carbon (BC) is instead , but chemical and optical properties of the dry particles are unaffected. Hydrophilic OM undergoes hygroscopic growth, while hydrophilic BC is optically identical to the hydrophobic type, which represents pristine soot monomers. In reality, aged BC appears in the form of clusters or chain-like aggregates (e.g. Teng et al. (2019) and references therein) that clump with hydrophilic sulfate (SU)SU, nitrate (NI) and ammonium (AM) salt particles to form highly-solublecrystals to form highly soluble, large structures. Observed OM also forms coatings around SU aerosol cores, eventually mixing with incorporating soot particles (Yu et al., 2019). While we cannot afford to fully address this fully address the ageing issue in this study, progressing toward more sophisticated representations of ageing processes might be a future area of improvements for CAMS, given the relevance of aging for determining CCN ageing for aerosol number concentrations and, ultimately, cloud droplet number concentrations. Aerosol sources depend on the species and N_d.

Aerosol sources can depend on meteorological forcing (SS, DU, SU precursors), chemistry (secondary OM, NI, AM, SU), natural and anthropogenic emissions (SU, AM, NI, OM), including wildfires (OM, BC). In turn, chemical processes also depend on the meteorology and radiative fluxes. Removal of aerosol particles takes place via a range of processes, the most of efficient being While all species undergo sedimentation and dry deposition, wet scavenging by precipitation . Each species has is the most efficient removal process for hydrophilic aerosols in models. IFS-COMPO assigns each species a fixed wet scavenging coefficient indicating the mass fraction to be considered assumed to be dissolved in cloud water; this value is 0.7 for all hydrophilic species except sea salt, for which it is fixed to SS (0.9and ammonium, for which it is) and AM (0.8(ECMWF, 2024a). When cloud water is converted to precipitation, the scavenging coefficient determines for each species how much of it shall be removed from the grid-box.) (ECMWF, 2024a). In mixed-phase conditions, a temperature-dependent modulation of the aerosol activated fraction from Verheggen et al. (2007) is applied to the precipitating ice-phase fraction of the cloud. In order to calculate the number concentration of available CCN from aerosol fields, a conversion from mass to number is neededwhen precipitating snow is produced.

Aerosol number concentrations can be obtained from mass concentrations with the number-to-mass ratio (J). For a given PSD of (spherical) particles, the ratio of particle numbers per unit mass J is given by: this is defined as

$$J = \frac{3}{4\pi\rho}\left(\int_{r_{\min}}^{r_{\max}} r^3 n(r)\,\mathrm{d}r\right)^{-1} \tag{2}$$

where the definite integral has an analytical solution when the domain coincides with the set of real numbers $\mathbb{R}$: where we explicated the dependency of the number-to-mass ratio on the median radius r_{med}. Thereby, each tracer definition defines a

map between the mass and number representation given by Equation 2. Observations ρ is the aerosol density, and r_{min} and r_{max} are the aerosol bin boundaries.

CAMS aerosols are routinely validated via observations of aerosol optical depth (AOD), particulate matter (PM) , and surface concentrations of speciated aerosols, as well as deposition fluxes are used to constrain aerosols in the IFS; . AOD is also operationally assimilated to produce CAMS analyses (Benedetti et al., 2009). However, these observed quantities offer very little most of these offer limited information about aerosol number concentrations. This is also the case for AOD, despite it depending on assumptions made on optics (refractive index), physical shape and PSD. To illustrate this for AOD, Figure 1 shows the dependency on r_{med} r_{med} of J together with the $500\ \text{nm}$ mass extinction coefficient (k_{ext}) for a selection of IFS aerosol tracers at different values of relative humidity, which was calculated using the Mie theory for spherical particles. In most cases, curves are quite flat at the default value of r_{med}, which means r_{med}, indicating that k_{ext} is almost independent of weakly dependent on small displacements of the PSD. This property derives from the fact that the population is characterises populations dominated by particles with radius r such the ratio $x = 2\pi\lambda/r$ in the visible regime is close to the peak $x \approx 6$ $x \approx 6$ of the Mie extinction efficiency (Petty, 2006). Relatively small rigid displacements of the PSD of species providing CCN generally have By consequence, relatively small changes of the aerosol PSDs have potentially negligible impact on k_{ext}, but large on J (1-2 orders of magnitude). The same holds also for small changes in the shape parameter σ (not shown). Given that Nonetheless, AOD in the visible range (400 to $800\ \text{nm}$) is a weak constraint for aerosol particle numbers number concentrations in a bulk representation. Therefore, we aim at making to make modest changes to the PSD assumptions of aerosols in order to optimize aerosol PSD assumptions to optimise the prediction of N_d, while keeping the setup physically consistent with the AOD currently simulated by the system.

3 Observations and Observational datasets

3.1 MODIS AOD and N_d

The The optimisation of aerosol PSDs presented in this work relies exclusively on MODIS N_d retrievals, while all other datasets (AERONET, CERES, VIIRS, MODIS AOD) are exclusively used for validation.

3.1 MODIS AOD

The MODerate Resolution Imaging Spectroradiometer (MODIS) is mounted on board the polar-orbiting Aqua and Terra satellites operated by NASA. For this study, we use monthly Collection 6.1 level 3 $550\ \text{nm}$ AOD observations covering the period 2003-2024 (Platnick et al., 2017a, b), produced with the Dark Target retrieval algorithm over land and sea (Levy et al., 2013; Sayer et al., 2014).

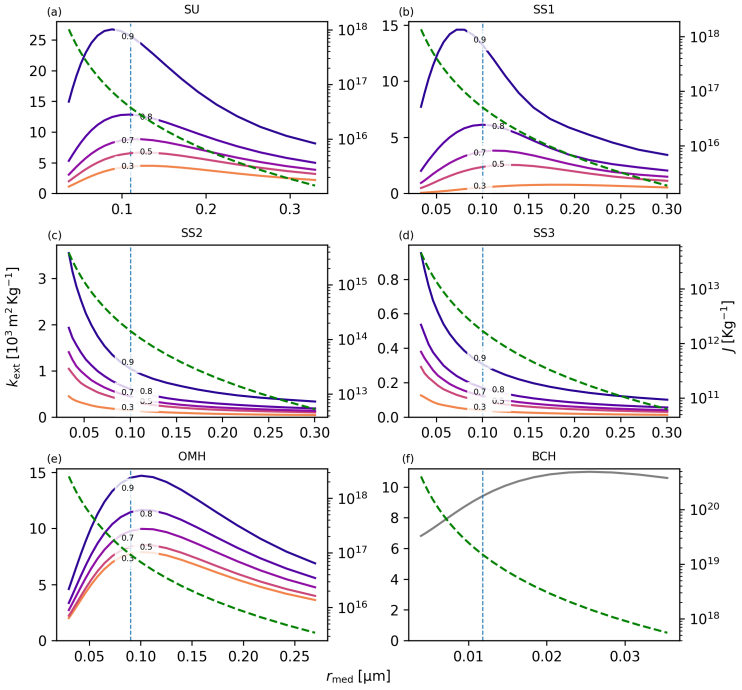

Figure 1. Mass extinction coefficient k_{ext} at 550 nm and number per unit mass J (as defined in Equation 2) as a function of the median radius r_{med} of the number PSD for the hydrophilic aerosol species listed in Table 1. Labels indicate curves corresponding to a selection of relative humidity values. Nitrates and ammonium are not shown, but their optical properties are very close to sulfates for the purpose of this discussion. The dashed green line shows the number of particles per unit mass J as a function of r_{med} and its scale is given on the right of each plot. For each tracer, the vertical dashed line indicates the default dry median radius according to Table 1. For sea salt, the ratio between the two modes median radii $r_{\text{med},2}/r_{\text{med},1}$ was kept constant, and the dashed line indicates the location of the finer mode.

3.2 MODIS N_d

We also use daily MODIS N_d retrievals (Gryspeerdt et al., 2022a) produced by combining Level 2 MODIS 2.1 μm retrievals of cloud optical thickness τ and cloud top cloud-top effective radius (r_e(Platnick et al., 2017c)) (Nakajima and King, 1990; Platnick et al., 2017c) under adiabatic (non-precipitating, non-mixing) cloud assumptions. The datasets are describe by Gryspeerdt et al. (2022b) and we used data for the period 2003-2020 on a $1^\circ \times 1^\circ$ rectangular grid. The N_d satellite products computed from bi-spectral retrievals of cloud optical thickness (τ) and effective radius (r_e) (Nakajima and King, 1990) assuming adiabatic profiles for stratocumulus clouds and only including pixels with values are retrieved only for liquid-phase clouds with cloud-top temperature more larger than 268 K (see Gryspeerdt et al. (2022b) and references therein). Each (Gryspeerdt et al., 2022b). There are several N_d dataset is the result of datasets included in Gryspeerdt et al. (2022a), each resulting from differ-

ent sampling strategies to target aimed at targeting systematic error sources affecting satellite retrievals. The least restrictive sampling strategy is labelled follows Quaas et al. (2006) (Q06) and selects pixels with retrieved effective radius (r_e) larger than $4\,\mu m$, and a minimum cloud optical thickness τ of 4. We also make use of two other sampling strategies from the Gryspeerdt et al. (2022b) paper. One is named $r_e > 4\,\mu m$ and $\tau > 4$. One follows Grosvenor et al. (2018b) (G18, which) and also requires a pixel cloud fraction larger than 0.9 as well as minimal thresholds for satellite and solar zenith angles, to address uncertainties errors associated with cloud measurements under slanted views (e.g. Maddux et al., 2010)(Maddux et al., 2010; Grosvenor et al., 2018b). The other one is follows Bennartz and Rausch (2017) (BR17, which,) and, on top of all the above-mentioned filters, also excludes all pixels for which the imposes a stacking order for $r_e$retrieval does not strictly , that must increase with the wavelength of the deployed near-infrared channel ($1.6\,\mu m$, $2.2\,\mu m$ or $3.6\,\mu m$) ; this was meant to discard non-adiabatic cloud profiles(see Gryspeerdt et al. (2022b) for a detailed discussion). For this study, we down-sampled the retrievals (.

We use the Q06, G18 and BR17) N_d retrievals averaged to monthly means and re-gridded them to a $3° \times 3°$ rectangular grid on the original $1° \times 1°$ rectangular grid for the period 2003–2020. We use Q06 as the tuning target , while we take the spread across the three datasets to estimate the uncertainty of observations. For each pixel, error bars are defined optimisation target due to its broader spatio-temporal coverage, and define error bars as the full dispersion (maximum minus minimum) of values spread across the three datasets . If data are missing in one of the datasets (because there are no valid retrievals satisfying the more restrictive sampling method), the assigned relative error is 1. By doing this we aim at producing error bars that reflect the sensitivity of N_d numbers on every strategy aimed at removing specific sources of error and use this as an indicator of the reliability of the retrieved values. at each grid-point. This approach captures sensitivity to known retrieval artifacts without assuming a specific error model.

3.3 VIIRS AOD and AE

The visible Visible Infrared Imaging Radiometer Suite (VIIRS) is mounted on board the Suomi National Polar-orbiting Partnership (SNPP) and NOAA-20 satellites, operated by NOAA. We use the Level 3 monthly $550\,nm$ AOD and $550\,nm - 865\,nm$ $550–865\,nm$ Angstrom exponent (AE) products for the period 2023-2024, produced with the Deep Blue (Hsu et al., 2013) retrieval algorithm over land and the Satellite Ocean Aerosol (SOAR) SOAR (Sayer et al., 2018) algorithm over sea. for the period 2023-2024(SSEC, 2023a, b). the ocean (SSEC, 2023a, b).

3.4 AERONET AOD, AE and size spectra

The Aerosol Robotic Network (AERONET) is an extensive network of ground-based sun photometers, providing measurements of aerosol optical properties (Holben et al., 1998). We use daily cloud-cleared, quality-assured and fully-calibrated fully calibrated (Level 2) AOD and AE products$550\,nm$ AOD and $440–870\,nm$ AE observations, as well as daily cloud-cleared, quality-controlled (Level 1.5) aerosol PSD inversion products (Dubovik and King, 2000) for a selection of observational sites. We used all data between 2003 and 2024 available for each site.

3.5 CERES EBAF TOA broadband shortwave fluxes

The Clouds and the Earth's Radiant Energy System (CERES) instruments for the measurement of top-of-atmosphere (TOA) broadband shortwave (SW) and longwave (LW) radiation (Wielicki et al., 1996) are mounted on board the Aqua, Terra, SNPP and NOAA-20 satellites. For this study we use TOA broadband shortwave (SW) all-sky monthly fluxes from Edition 4.2 Energy-balanced Energy-Balanced and Filled (EBAF) dataset (Doelling, 2022) for the period 2023-2024.

4 Method

We constrained aerosol numbers This study on ACI considers only the first indirect aerosol radiative effect, excluding any direct impact on cloud lifetime. This choice focuses on the activation pathway, without the introduction of additional feedback mechanisms, and reflects the more limited understanding of the effect of aerosols on precipitation compared to the first indirect and the semi-direct radiative effect (Stier et al., 2024). Moreover, if lifetime effects were active, the optimisation problem would no longer be well-defined, as N_d changes would directly affect precipitation and cloud evolution, while the optimisation relies on stored cloud fields. This section presents how we constrain aerosol number concentrations for the bulk IFS representation with satellite retrievals of droplet number concentrations (N_d). Thereby, we used If N_i indicates the number concentration of the i-th aerosol species of a set of p species and assuming that, for each species, all particles larger than a critical size activate into droplets, N_d observations as a tuning target for the N_d values obtained by activation of hygroscopic aerosol species. In ordercan be written as

$$N_d = \sum_{i=1}^{p} N_{d,i} = \sum_{i=1}^{p} \alpha_i N_i \tag{3}$$

where $N_{d,i}$ indicates the number of activated particles and α_i the activation rate for the i-th species, as a general function of the local atmospheric composition, thermodynamics and dynamics. In terms of relative changes for a given species i:

$$\frac{\mathrm{d}N_{d,i}}{N_{d,i}} = \frac{\mathrm{d}\alpha_i}{\alpha_i} + \frac{\mathrm{d}N_i}{N_i} \tag{4}$$

Now we can estimate how a finite change in the median radius r_{med} can affect N_d. Let's consider as an example sulfate aerosol (frequently a dominant CCN provider) and a change in its PSD r_{med} from $0.10\,\mu\text{m}$ to achieve this, we firstly implemented a $0.08\,\mu\text{m}$. This will affect N_d by changing both the activation rate α_i and the particle number concentration N_i. The change in α_i derives from r_{med} determining the critical supersaturation (S_{crit}) distribution and thus the maximum supersaturation during ascent. Using results from Rothenberg and Wang (2016), we estimate $|\frac{\Delta\alpha_i}{\alpha_i}| \lessapprox 0.2$. Rothenberg and Wang (2016) report that r_{med} is also the largest controller on activation rates α_i, so that we can neglect from now on the potential effect of changing the geometric standard deviation σ and the hygroscopicity κ. The effect of the r_{med} change can be then estimated using Equation 2 in the approximation of $r_{\text{min}} = 0$ and $r_{\text{max}} = \infty$: $\Delta N_i/N_i \approx \Delta J/J \approx -3\Delta r/r$, so that $|\Delta N_i/N_i| \approx 0.6$. Thus, the aerosol PSD median radius r_{med} exerts the strongest control on N_d through N_i, and secondarily through α_i. This ensures that, to a first order, we can estimate the impact of r_{med} on N_d by neglecting the impact of r_{med} on the S_{crit} curve, i.e. by avoiding new parcel ascent computations and keeping α_i constant. In addition to r_{med}, α_i is controlled by the updraft velocity w (Rothenberg and Wang, 2016), which is the only environment quantity that we will diagnose for estimating N_d.

On the basis of these premises, we implemented a simple and lightweight scheme to simulate aerosol activation into droplets that could diagnose N_d that relies on a lookup-table (LUT) of pre-simulated parcel simulations. Such a scheme can be used either by the online when running the IFS (online) or or offline on stored data (offline). to infer N_d from local aerosol fields and environmental variables such as vertical velocity. Section 4.1 describes its design and interface with the IFS radiation scheme. Section 4.2 describes model data and processing used for the online N_d simulations and Section 4.3 describes the offline optimisation procedure.

4.1 Activation The aerosol activation scheme for the IFS

The activation process of a population of aerosol particles can be summarized in such a way that, depending on local aerosols and thermodynamics (supersaturation) , thermodynamics (S_{sat}) and kinetics (timescales of ascent and water vapor condensation), for each species all particles larger than a critical size activate into a droplet. In order to describe the number concentration of droplets we need the number PSD of each CCN species By consequence, to describe N_d the number PSD description is needed, while to compute the mass eventually scavenged by cloud formation (only with prognostic aerosols) we need scavenged by precipitation their mass PSD . Figure **??** shows particle number and volume (or, equivalently, mass , as we consider one value of density for is required. Depending on the aerosol species and cloud regimes, it might be consistent to assume low variability for mass activated fractions (as done by the IFS-COMPO by assigning a prescribed value to each species) PSDs and the associated range of dry critical radii under typical atmospheric conditions for boundary layer stratocumuli obtained from parcel simulations (details are provided below). These translate directly into activated mass and number fractions. For sulfates we expect large variability in the number of particles activating into droplets (between 10% and 90%) but small variability in the amount of mass dissolved (between 80% and 100%). For aged black carbon, due to the lower hygroscopicity and smaller typical particle size, we expect the opposite configuration of variability, very small in activated numbers, much larger in activated mass fractions. The while still diagnosing a variable number activated fraction.

We used the adiabatic parcel ascent model by Rothenberg and Wang (2016) (Pyrcel) is used to simulate activation of a heterogeneous population aerosols particles. The same parcel model has also been used by Fossum et al. (2020) to investigate the effect of large sea-salt particles to reduce the activation efficiency of sulfate CCN. Results of offline simulations are stored heterogeneous aerosol particle populations.

We stored the results of the offline simulations into a lookup table (LUT) that takes as input the inputs the parcel updraft velocity and the number concentration of a set of pre-defined CCN species and provides CCN-providing aerosol species and yields number and mass activated fractions, as well as critical dry radii. Atmospheric variables for the simulated activation describe a are set to describe air parcel ascent with initial pressure $850\,\mathrm{hPa}$, temperature $278\,\mathrm{K}$ and 98% relative humidity, being lifted for lifted for a minimum of $100\,\mathrm{m}$ at $1\,\mathrm{m/s}$. There is no until peak S_{sat} is reached.

Previous studies found weak dependency of the LUT on atmospheric variables other than aerosol number concentrations. Vertical velocity is known to have a relevant impact on activated particle numbers, especially in regimes with activation process on cloud-base pressure and temperature, especially for warm phase regimes (above 273 K) (Leaitch et al., 1986; Rothenberg and Wang, 2016). We perform simulations for a range of vertical velocities w (updrafts) to precisely describe also regimes with relatively high CCN concentrations (greater than $1000\,\mathrm{cm}^{-3}$- so called updraught-limited) (Pruppacher and Klett, 2010; Reutter et al., 2009; Rothenberg and Wang, 2016; West et al., 2014). However, diagnosing accurate sub-grid vertical velocity and variability in a hydrostatic model with a purely-diagnostic description of turbulence can be quite a challenge; this also poses the risk of introducing significant noise in the results, rendering the identification of major sources of error, namely aerosol number concentrations, more difficult in such a first implementation of the activation scheme. Therefore, the simulations are done for every combination of number concentration for each species over 7 geometrically-spaced values, using a fixed vertical

Name	κ	r_{med} (µm)	σ	N (cm^{-3})	Recipe
sulfate (Sul)	0.54	0.11	1.6	$[10, 1000]$	$1m_{\text{SU}}$
nitrate (Nit)	0.88	0.035	2.0	$[5, 500]$	$1m_{\text{AM}} + 0.62m_{\text{NIF}}$
sea salt fine (Ssf)	1.10	0.01	1.9	$[3, 300]$	$1m_{\text{SS1}} + 0.05m_{\text{SS2}}$
sea salt coarse (Ssc)	1.10	0.1	2.0	$[0.02, 20]$	$1m_{\text{SS3}} + 0.95m_{\text{SS2}}$
organic (Org)	0.07	0.09	2.0	$[1, 1000]$	$1m_{\text{OMH}} + 0.7m_{\text{SOA}} + 0.7m_{\text{SOB}}$
soot (Soo)	0.07	0.0118	2.0	$[5, 5000]$	$1m_{\text{BCH}}$

Table 2. Definition of CCN-providing species. For each species the hygroscopicity κ as well as the median radius r_{med} and shape parameter σ of the log-normal distributions are listed. The column labelled with N reports the range of number concentrations considered; within this range, 7 geometrically spaced values are used for the Pyrcel simulations. Recipes are reported as mass mixtures of the IFS-COMPO species denoted by m_x, where x refers to species reported in Table 1. The scaling factors for each aerosol species are defined by the number-to-mass ratio J (see Equation 2) associated with the CAMS default PSDs, such that the number contribution from each tracer is conserved when forming the mass mixtures.

velocity of 1 m/s as representative for boundary layer mixing velocities (Hogan et al., 2009), resulting in 117649 simulations. In order to , updraft-limited) (Pruppacher and Klett, 2010; Reutter et al., 2009; Rothenberg and Wang, 2016; West et al., 2014; Sullivan et al., 2016). To keep the number of simulations lowmanageable, we define a small set of 6 internally-mixed CCN CCN-providing aerosol species derived from aerosol species defined those in Table 1, by grouping together those with similar size and species with similar physico-chemical properties and assigning hygroscopicity κ reflecting typical values with typical values inferred from Petters and Kreidenweis (2007). The CCN species used for the offline activation simulations, as well as the definitions mapping the IFS aerosols into the CCN species (recipes) are listed Their definitions are reported in Table 2. Results of the activation process are stored in a lookup table (LUT) as critical dry activation radii,as well as corresponding activated number and mass fractions. We performed activation simulations for every combination of number concentration for each species and vertical velocity (between $0.1\ \text{m s}^{-1}$ and $10\ \text{m s}^{-1}$) over seven geometrically-spaced values resulting in a total of 823,543 simulations. Subsequently, these results were integrated over Gaussian distributions of vertical velocities with seven values of mean $\bar{w}$ in the range $[-0.2\ \text{m s}^{-1}, 0.2\ \text{m s}^{-1}]$ (symmetric around zero, absolute values geometrically spaced) and seven geometrically-spaced values of standard deviation σ_w in the range $[0.05\ \text{m s}^{-1}, 2.5\ \text{m s}^{-1}]$. The integration is performed only for $w > 0$ as in Golaz et al. (2011). The final size of the LUT is of 5,764,801 elements.

The LUT yields activated number fraction (a_x) for each CCN-providingspecies x listed in table 2 given a Table 2 for a given mixture of particles . Such values are used to compute the amount of aerosol particles activated into droplets for each species. The and configuration of $\bar{w}$ and σ_w. The activation scheme is in this sense a wrapper of the LUT accessor with pre- and post-processing capabilities, that extracts the nearest-neighbor value along the aerosol concentrations dimensions, and linearly interpolates along the $\bar{w}$ and σ_w dimensions. As a final step, the scheme computes the number of droplets N_d is defined as the sum of the activated particles across all CCN species. The LUT using Equation 3 and returns it to the caller. The diagnosed N_d can be used either online by the IFS 's radiation scheme to compute the liquid droplets r_e in liquid-phase clouds. (see below).

Similarly, the LUT can be accessed offline to estimate N_d from a given aerosol population and updraft conditions. When running the IFS with prognostic aerosol tracers, the activation scheme can also be called a second time by the wet deposition code to diagnose the activated mass fraction for each hydrophilic species. Similarly, the LUT can be invoked offline to estimate

4.2 Activation scheme in the IFS (online)

The IFS (CY49R1) has a single-moment cloud microphysics scheme with prognostic variables for cloud fraction and water content for cloud liquid (LWC), cloud ice (IWC), rain (RWC) and snow hydrometeors. The radiation scheme diagnoses r_e needed for the all-sky radiative calculations:

$$r_e = \left[\frac{4(\mathrm{RWC}+\mathrm{LWC})}{3\pi\rho_w\gamma N_d}\right]^{1/3} \tag{5}$$

where $\gamma = \left(\frac{r_v}{r_e}\right)^3$, with r_v mean volumetric ratio, ρ_w is the density of water and N_d from a given aerosol population.

4.3 Model data selection

Aerosol fieldswere the cloud droplet number concentration.

The IFS uses a wind-dependent parametrisation derived from Martin et al. (1994) such that, for 10-m winds between 0 and $10\ \mathrm{m\,s^{-1}}$ $N_d \in [40\ \mathrm{cm^{-3}}, 70\ \mathrm{cm^{-3}}]$ over the ocean and $N_d \in [140\ \mathrm{cm^{-3}}, 170\ \mathrm{cm^{-3}}]$ over land. γ derives from the studies by Martin et al. (1994) and Wood (2000), and uses the values of 0.77 over ocean and 0.69 over land, with adjustments to represent increased dispersion of the cloud droplet PSD when drizzle is present. We redirect the reader to the IFS documentation (ECMWF, 2024b) for further details.

In the setup for this study, the IFS radiation scheme can diagnose N_d with a call to the activation scheme described above by providing as input $\bar{w}$, σ_w and aerosol mass concentrations of all aerosol species required to construct the CCN providers of Table 2. $\bar{w}$ is set equal to the large-scale vertical velocity, which is typical for climate models (Ghan et al., 2011; Van Noije et al., 2021). σ_w for turbulent boundary layers is generally diagnosed from turbulent kinetic energy (TKE) or eddy diffusivity (Ghan et al., 2011); however, these are not available as ERA5 fields, therefore for this study we used the Deardorff velocity scale w^* for convective boundary layers (Deardorff, 1970), scaled by a factor 0.6 to diagnose σ_w, in line with relationships found in observations and numerical simulations (Deardorff, 1970; Hogan et al., 2009). A minimum value of $\sigma_w = 0.1\ \mathrm{ms^{-1}}$ is imposed to ensure physical activation conditions (e.g. Golaz et al., 2011; Barahona et al., 2014).

Autoconversion rates of cloud water to rain are computed using the parametrisation from Khairoutdinov and Kogan (2000) assuming fixed N_d values over land and sea, and this behaviour is left unchanged within this study, so that our setup does not have any direct impact of aerosols on cloud lifetime.

4.3 Activation scheme stored fields (offline)

To perform the offline N_d computations needed by the optimisation procedure we relied on stored aerosol fields originally produced for verification purposes from lower resolution (triangular-linear TL255, ≈ 38 km≈ 78 km) CAMS 1-day forecasts initialized from ECMWF reanalysis C3S (2018) v5 (using initial conditions from ERA5) (Hersbach et al., 2020) over the period 2003-2020, and 2003–2020. Evaluations of the CAMS aerosol system (with and without assimilation of observations) can be found in Rémy et al. (2022) and in the CAMS validation reports released periodically (see e.g. Blake et al. (2025)); near real-time validations are also publicly accessible using tools such as Aeroval (https://aeroval.met.no, accessed April 2026). Simulated aerosol fields were stored on 16 pressure levels between 10 hPa and 1000 hPa. The ; the 11 pressure levels below 100 hPa levels have thicknesses ranging between ≈ 640 m and ≈ 2300 m, with the highest resolution found in the lower troposphere and lowest resolution in the mid-troposphere. Such low vertical resolution is clearly suboptimal for the purpose of extracting accurate aerosol concentrations at cloud level; however, recycling these data allows using these data enables us to get useful insights on the current state of the model climate and the potential of the tuning procedure, without needing to re-run a rather computationally-expensive simulation. optimisation procedure, which we also expect to partially compensate for resolution-driven inaccuracies.

4.4 Model data selection for the offline optimisation

We extracted from ERA5 the following meteorological fields for the period 2003-2020 on model levels2003–2020: pressure (p), temperature (T), cloud cover (f), liquid (LWCLWC) and ice (IWCIWC) water content. Meteorological data These cover the lowest 57 of the 137 IFS model levels, which correspond to up to 10 km altitudein the International Standard Atmosphere. For each data stream we select within each month every fifth day starting the third day of the month; for each day, we take the use 3-hourly data (00, 03, 06, 12 and 18 UTCtime-steps..., 21 UTC). All fields are interpolated on a rectangular $3^\circ \times 3^\circ$ grid. In order to find CAMS aerosol concentrations at the cloud level, we consider only to the same $1^\circ \times 1^\circ$ grid of the N_d retrievals datasets.

For each column, only points with local time between 09:30UTC and 15:30UTC, to reflect the typical daytime overpasses of the Aqua and Terra satellites. Only cloudy model grid-boxes are then retained, defined as those with at least 10% cloud fraction. For each column, we estimate the cloud optical thickness τ across all cloudy grid-boxes and keep only those columns for which $\tau > 4$. The formula used is: where $\gamma = \left(\frac{r_v}{r_e}\right)^3 = 0.8$ is the ratio between mean volumetric (r_v) and effective (r_e) radius and Δz_k the geometrical thickness of the layer. N_d in equation **??** is set to 70 cm^{-3} over land and 170 cm^{-3} over sea, as estimates for N_d yielded by the wind-dependent parametrization of the IFS when the 10 m wind speed is ≈ 10 m/s. The representative cloud top level is the one for in line with Quaas et al. (2006).

We define the representative cloud-top level as the level at which the cumulative optical thickness computed from the top of the clouds crosses the threshold of 2 $\tau = 2$ and the cloud bottom as the one for which the cumulative cloud optical thickness crosses the value of where it reaches 95% of the total cloud optical thickness τ. We select warm-phase clouds by only keeping cloudy columns for which the temperature at cloud top is larger than 268 K, and for which the ratio of ice to total cloud

water is below 0.5. By doing this, we aim at selecting data points where both the model and MODIS see Optical thickness is diagnosed offline assuming a constant extinction efficiency of $Q_{\text{ext}} = 2$. We chose the cloud-top threshold for consistency with MODIS cloud-top properties being typically within $\tau \approx 1$ in the infrared (Wang et al., 2014a), given that the extinction efficiency for wavelengths of $\approx 10\,\mu\text{m}$ in liquid clouds is between 1 and 2 (Mitchell, 2000). Stratocumulus clouds also have optically thick and geometrically sharp cloud tops, spanning several units of optical thickness within one model level, which makes the results relatively insensitive to the precise choice of the optical thickness threshold for cloud-top identification. For completeness, we tested the sensitivity to cloud-top threshold values of $\tau = 1$ and $\tau = 7$, consistent with bounds provided by correction formulas in Grosvenor et al. (2018a) for r_e retrievals. This affected cloud-top height location by less than 30 hPa for the thickest clouds, and produced variations within 0.7% in the global loss function (see below for its definition). Within a cloudy model column, we select liquid-phase stratocumulus clouds . Note that clouds as those where at cloud top $T > 268$ K, and $\text{IWC}/(\text{LWC} + \text{IWC}) < 0.1$ similarly to the observational filtering criteria, but allowing for some ice within the gridbox due to the coarse resolution of the model fields ($3° \times 3°$) , we adopted selection criteria that are more relaxed than those used for the $1° \times 1°$) compared to the level-2 data the N_d retrievals. datasets were derived from (Gryspeerdt et al., 2022b).

For a cloud layer with constant N_d profile, equation **??** yields the instantaneous the instantaneous finite relative change in τ obtained by changing a change in N_d: which describes the impact of aerosols on N_d , assuming all other variables staying the same similarly to Twomey (1991). This formula assumes constant unchanged (Twomey, 1991) is given by $N_d^{1/3}$ scaling, while the relationship with $\Delta N_d/N_d$ holds only for small perturbations:

$$\frac{\Delta\tau}{\tau} = \frac{\Delta N_d^{1/3}}{N_d^{1/3}} = \frac{1}{3}\frac{\Delta N_d}{N_d} + \mathcal{O}\left(\frac{\Delta N_d}{N_d}\right)^2_{\Delta N_d/N_d \to 0} \tag{6}$$

Throughout this study we set $\gamma = 0.8$ consistently with the N_d distribution width, represented by the parameter γ in Equation **??**. While γ has potentially a retrieval methods by Gryspeerdt et al. (2022b). Despite the potentially regime-dependent (Wang et al., 2023) impact on cloud albedo, as well as autoconversion of cloud water to precipitation (Liu et al., 2006), impact of γ on cloud microphysics (Liu et al., 2006; Wang et al., 2023), there is currently no settled knowledge about how such parametrization for γ should be used for global observations and modelling. One can incorporate the effect of on how this parameter should be represented in models.

However, typical errors of assuming a fixed value for γ on τ by rewriting equations **??** and 6 as functions of an effective droplet number concentration $N_e \equiv \gamma N_d$. Since typical errors in γ are estimated between 10% and 14% (see Grosvenor et al. (2018a) and references therein), this would produce which translate into a relative error in τ within approximately 4%. , which we show below to be of secondary importance to that induced by aerosol number concentrations.

4.5 Optimization The offline optimisation procedure

Aerosol mass concentration fields are interpolated at the representative cloud top At each stored time and for every column of the domain, we interpolate aerosols to the identified cloud-top level p and converted to calculate aerosol number concentrations using equation 2. The Equation 2. Given the relatively low vertical resolution of the aerosol dataset, the extracted population at cloud level represents a vertically smoothed average of actual simulated populations above and below the cloud level. The

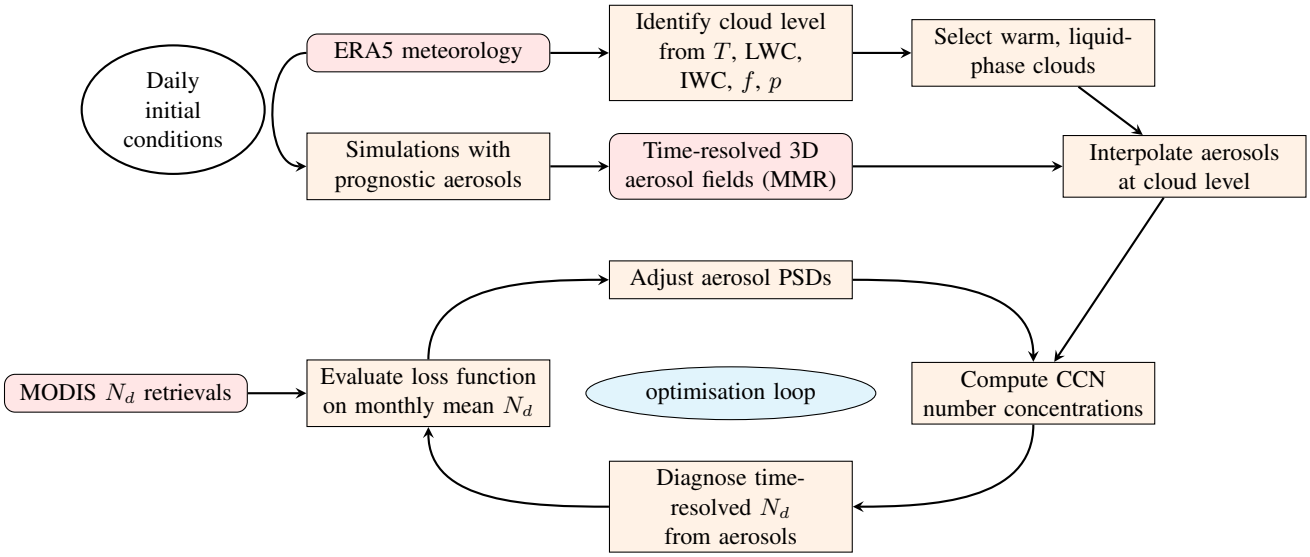

Figure 2. Flowchart of the optimisation procedure used to adjust aerosol particle size distributions (PSDs). This is performed over a time window of 1 year for each of the 18 years of the study.

activation LUT is then used offline to compute the corresponding as a mapping function to diagnose $N_{d,\mathrm{IFS}}$ diagnostics. Such simulated values are then compared with the observed values from local aerosols and vertical velocity diagnostics. These are then averaged to monthly data, using only locations with at least three identified warm-phase cloud cases within the month. For each year, the simulated monthly-mean N_d are evaluated against the observed monthly-mean $N_{d,\mathrm{Q06}}$ fields using the following loss function $\mathcal{L}$:

$$\mathcal{L}(N_{d,\mathrm{IFS}}) = \left|\left| \frac{N_{d,\mathrm{IFS}}^{1/3} - N_{d,\mathrm{Q06}}^{1/3}}{\Delta \tilde{N}_{d,\mathrm{MODIS}}^{1/3}} \right|\right|_2 \tag{7}$$

$$\Delta \tilde{N}_{d,\mathrm{MODIS}}^{1/3} \equiv \max_{\mathrm{Q06,G18,BR17}} N_d^{1/3} - \min_{\mathrm{Q06,G18,BR17}} N_d^{1/3} \tag{8}$$

where the writing $N_{d,y}$ uses y to indicate either the simulated $||\cdots||_2$ indicates the area-weighted average on the spherical surface and the source of N_d can be the offline diagnostics (IFS) values or one of the three sampling strategies for MODIS N_dMODIS sampling strategies: Q06, G18, BR17 (Gryspeerdt et al., 2022b). Here we implicitly assume that the spread across the different sampling strategies is representative of the error variance to be associated to retrievals. $||\cdots||_2$ indicates the Euclidean norm on the gridded space including weighting the grid area by the cosine of latitude. The optimization procedureis illustrated by the flowchart in Among the retrievals, $N_{d,\mathrm{Q06}}$ is chosen as the optimisation target since Q06 is the least restrictive sampling strategy, which implies the largest number of valid retrievals.

As an optimisation algorithm for the loss function $\mathcal{L}$ we use Nelder-Mead with free bounds, a popular minimisation method belonging to the class of direct search methods, i.e. that do not require knowledge of the gradients of the function, for functions of the kind $f(\mathbb{R}^n) \to \mathbb{R}$, which is the case for the constructed $\mathcal{L}$. The algorithm uses n-dimensional convex hulls and performs

a series of reflection, expansion and contraction operations to converge on function minima (see e.g. Lagarias et al., 1998). Over the many setups used for the optimisation procedure, we never encountered important convergence issues.

The optimisation procedure is illustrated in the flowchart of Figure 2. For each year from 2003 to 2020, $\mathcal{L}$ is evaluated by simulating on monthly N_d providing as an input to the LUT the using aerosol number concentrations computed using equation from Equation 2. The procedure is repeated in a loop leaving the median radius r_{med} as a free parameter for each CCN species excluding the coarse sea salt mode (seasalt2Ssc), for which the median radius is fixed as $10\, r_{\mathrm{med,seasalt1}}$. The optimization algorithm is Nelder-Mead with free boundsto $10\, r_{\mathrm{med,ssf}}$.

While aerosol and cloud data are spatially co-located, only monthly mean values are compared, so that $\mathcal{L}$ can be seen as a statistical evaluation of the simulated N_d. This implies that the optimisation targets large-scale and seasonal N_d signals, with variability on monthly or longer timescales. As a result, a collection of optimized the sensitivity to the co-location in time and space of cloud fields and satellite overpasses is reduced. At the same time, by considering a smaller number of samples within each month we can substantially reduce the amount of data processed, keeping the procedure manageable.

As a result, a collection of optimised median radii for each species x and year y is obtained, $r_{\mathrm{med},x,y}$. We finally define the optimal PSD as the one using the optimal median radius $\overline{r_{\mathrm{med},x}} \equiv \mathrm{med}_y(r_{\mathrm{med},x,y})$, i.e. the median across the 18 years of the optimized optimised median radii. Within this framework, the resulting optimised aerosol PSDs are constrained by the cloud-top N_d observations and represent an effective description of aerosol number consistent with these observations; their realism is conditioned by non-represented processes (e.g. diagnostic representation of N_d and absence of prognostic droplet microphysics) and aerosol biases (e.g. speciation and vertical structure), and is therefore evaluated *a posteriori* through independent observations of aerosol optical properties.

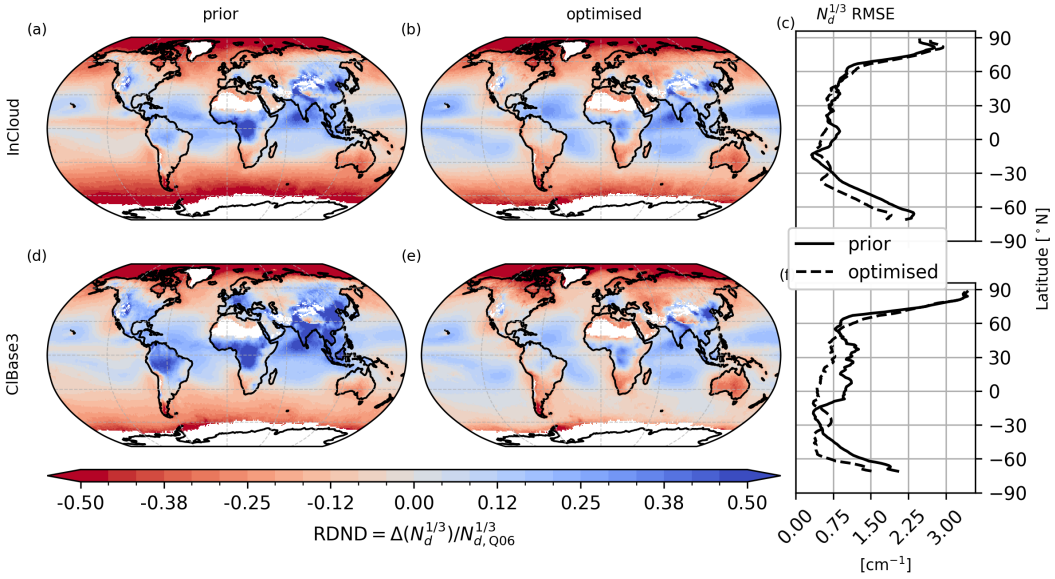

Figure 3. Offline-simulated mean N_d for the 18-year-period of optimisation from prior (IFS-COMPO default) (a, d) and optimised (b, c) aerosol PSDs, shown both in relative differences in $N_d^{1/3}$ (RDND) maps (a, b, d, e) and zonal $N_d^{1/3}$ RMSE (c, f) with respect to the MODIS N_d optimisation target, Q06. These are for the optimisation setups InCloud (aerosols diagnosed at cloud level - panels a, b, c) and ClBase3 (aerosols diagnosed three model levels below cloud base - panels d, e, f). Positive differences indicate that MODIS N_d (Q06) values are higher than those simulated.

Region	Domain
North Tropical Africa (NTA)	350°E-35°E, 5°N-15°N
Central Africa (CAF)	15°E-35°E, 10°S-5°N
Mid-Atlantic (MAT)	330°E-5°E, 20°S-0°S
Southern Indian Ocean (SIO)	20°E-100°E, 50°S-30°S
North Tropical Pacific (NTP)	130°E-210°E, 10°N-30°N
Southern Pacific (SOP)	180°E-280°E, 50°S-30°S
Europe (EUR)	355°E-25°E, 35°N-65°N
India (IND)	70°E-90°E, 5°N-30°N

Table 3. Domain definitions for regional N_d evaluation.

5 Results of the N_d optimizationoptimisation

Table 4 reports the result of the optimization procedure for each CCN species in terms of the optimal median radius and the implied number scaling. A major aspect is the reduction in the CCN number per unit mass J of nitrate ($\times 0.36$)and organics($\times 0.19$), while J for sea salt is increased ($\times 3.25$). The optimized PSDs globally improve the simulated N_d, with a 16.5% reduction of the prior evaluation of the loss function (Equation 7)from 1.98 to 1.65. Figure 3 shows the results of the optimization procedure by comparing simulated and observed $N_d^{1/3}$ values; the reason behind this choice is that relative changes in $N_d^{1/3}$ are representative of the instantaneous impact on cloud optical thickness τ, as illustrated in Equation 6. This shows that the optimization procedure significantly improves many open sea low- and mid-latitude regions characterized by typically low CCN concentrations, especially over the Pacific and the extratropical South Atlantic and Indian Ocean. Figure 3 also highlights a few regions that are recalcitrant to the optimization procedure and that are discussed more in detail below: simulated This section reports the outcome of the optimisation for three setups: a first one diagnosing N_d are biased high over the subtropical Pacific (Hawaii) and tropical sub-Saharan Africa, and biased low over the Southern Ocean. MODIS from aerosols found at the cloud-top level (InCloud, Section 5.1), a second one excluding BC from the CCN species (InCloudNoBC, Section 5.2), and a third one using aerosols found three levels below the cloud base (ClBase3, Section 5.3). Although CCN activation mainly occurs at cloud base, the model does not represent aerosol as explicitly dissolved within cloud droplets. The aerosol at cloud top has nevertheless been transported there by the same turbulent, mixing and advection processes that transport cloud water. In that sense, the aerosol population co-located with cloud droplets at cloud top (InCloud) provides a first-order diagnostic representation of the aerosol consistent with cloud-top $N_d$retrievals are known to suffer from an optical penetration bias due to the assumption that the spectrally-retrieved r_e values are representative of the PSD of cloud droplet at cloud top, which leads to overestimated retrieved , despite activation occurring at cloud base. The InCloudNoBC and ClBase3 setups are presented to check the robustness of the procedure to the CAMS BC representation and to the aerosol vertical profiles. Finally, we report in Section 5.4 the results of offline aerosol optics (speciated AOD and AE) simulations using prior (CAMS default) and optimised (InCloud) PSD.

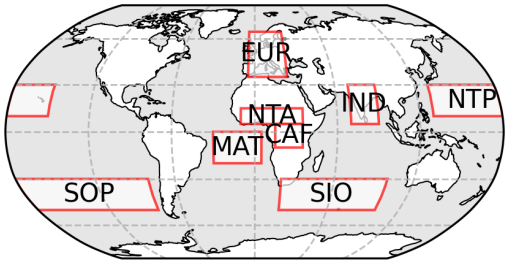

Figure 4. Map of regions defined in Table 3.

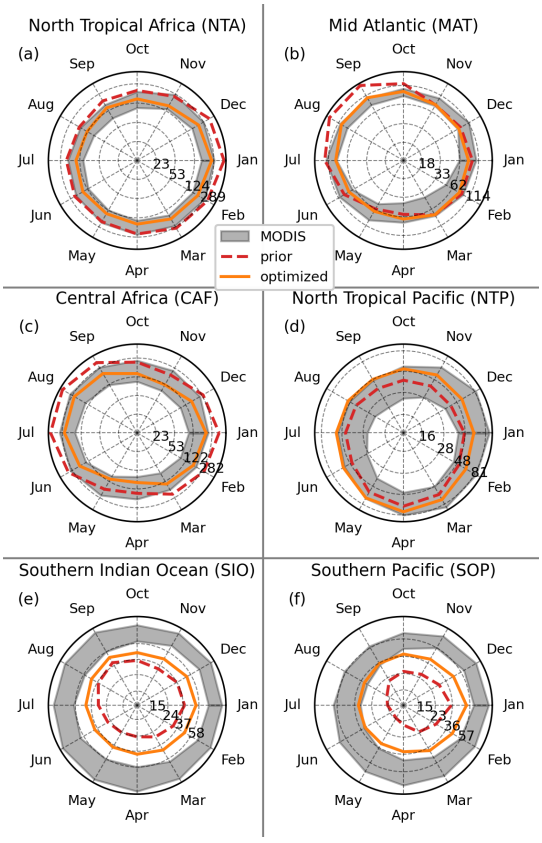

Figure 5. Simulated and observed monthly N_d (in units of cm^{-3}) for the NTA, NTP, CAF, SOP, MAT, SIO regions (see Table 3 and Figure 4) over the 2003–2020 period. Simulated values correspond to the CAMS default PSDs (prior) and the PSDs resulting from the InCloud optimisation setup (optimised). Shaded areas indicate the range of mean values spanned by the MODIS N_d datasets (see Equation 8). Note that the scale of N_d values is nonlinear.

5.1 N_d from cloud-top aerosol (InCloud)

The optimal median radii and implied number scaling for all three optimisation setups are reported in Table 4, while Figure 3 shows how the simulated N_d values. Grosvenor et al. (2018a) quantify such penetration bias N_d for retrievals at 2.2 µm at 50% or less for clouds with $\tau_c > 4$, while Gryspeerdt et al. (2022b) found that bias-correcting retrievals improves agreement with in-situ measurements for the VOCALS and E-PEACE campaigns, targeting the subtropical stratocumulus clouds off the coasts of Peru and Namibia. Such penetration bias is within 15% when evaluated in $N_d^{1/3}$ space and typically around 10% over open sea regions within 30° latitude, which may partially explain the discrepancy between overpredicted and observed N_d values using the prior definitions. At latitudes higher than 60°N and 45°S our method struggles at getting N_d high enough compared with observations. MODIS cloud retrievals are known to suffer from viewing geometry errors with large satellite and solar zenith angles (Maddux et al., 2010; Grosvenor and Wood, 2014), which could in principle degrade high latitude observations; such effects are included in one of the sampling strategies and contribute to defining the error bars that we associated with the MODIS observations. According to Gryspeerdt et al. (2022b), at latitudes larger than 60° such errors are positive and small, on average within $16\ \mathrm{cm}^{-3}$, which could still be relevant in relatively pristine regions over sea, with typical retrieved N_d values between $75\ \mathrm{cm}^{-3}$ and $100\ \mathrm{cm}^{-3}$. However, this only partially explains the low bias in simulated N_d at high latitudes. Figure 6 shows how using the optimized PSDs would impact simulated AOD, with mass concentrations staying constant. On a zonal mean, the new definitions for sea salt and nitrates tend to slightly increase AOD, with a larger relative impact at mid- and high latitudes in the Southern hemisphere. Despite the drastic change in simulated CCN number concentrations from using the optimized PSDs, the mean and local impact (not shown)on total visible AOD remains within a 10% range from the current definitions. Once again, this shows that aerosol PSDs are not well constrained by the need to correctly simulate their direct effect. Simulated AE is potentially more deeply affected by re-defined PSD, but for this scenario the impact is generally neutral. Degradation in simulated AE is verified between 10°N and 45°N and is due to the combined signal of SS, SU, NI aerosol and advected Mineral Dust over the Atlantic.

5.2 Tropical Nd

Using the default CAMS definitions leads to globally too low N_d associated with sulfate CCN over oceans. The optimization procedure results in a reduced PSD r_{med} for this species from 0.11 µm to 0.09 µm. Interestingly, the PSD for Sulfate aerosol was updated in IFS-COMPO CY49R1 $r_{\mathrm{med}} = 0.0355$ µm and $\sigma = 2.0$. Indeed, compare with the CY48R1 PSD definitions tended to overestimate Sulfate-associated CCN numbers by a factor 2.7 (not shown) optimisation target ($N_{d,\mathrm{Q06}}$) before (prior, CAMS default PSDs) and after optimisation (optimised), while these are underestimated by a factor $1/1.74 = 0.57$ with the new PSD definitions for the InCloud and ClBase3 setups. These are represented as relative differences in $N_d^{1/3}$, defined as

$$\mathrm{RDND} = \frac{\Delta N_d^{1/3}}{N_{d,\mathrm{Q06}}^{1/3}} = \frac{N_{d,\mathrm{Q06}}^{1/3} - N_{d,\mathrm{IFS}}^{1/3}}{N_{d,\mathrm{Q06}}^{1/3}} \tag{9}$$

which serves as a proxy quantity for expected first-order relative changes in τ (see Equation 6). The absolute zonal-temporal $N_d^{1/3}$ RMSE are also shown in Figure 3.

Optimal PSDs resulting from the InCloud setup imply reduced number per unit mass J of nitrate (Nit, $\times 0.69$) and organics (Org, $\times 0.08$) CCN species but increased for sulfate (Sul, $\times 1.11$) and fine sea salt (Ssf, $\times 3.96$) (see Table 4). Generally speaking, the IFS-COMPO aerosol scheme does not represent any change in aerosols PSD over time, and for binned species like SS and DU, no transfer of mass between bins is allowed (ECMWF, 2024a). However, mass transfer from Aitken ($r \approx 0.04$ µm)to accumulation ($r \approx 0.1$ µm) mode has been assessed by observations in tropical marine regions, and is likely driven by the incorporation of soluble aerosols in non-precipitating boundary-layer clouds (Hoppel et al., 1990). Both Aitken and accumulalation modes for sulfates have been for long time deployed in the Met Office Unified Model (Jones et al., 2001), with a typical local mass apportionment between Aitken and accumulation mode by 1:10 (Mulcahy et al., 2014). The general underestimation of The optimal PSDs globally improve the simulated N_d (see Figure 3), which corresponds to a reduction of the prior evaluation of the loss function $\mathcal{L}$ (Equation 7) by 13%, from 1.85 ± 0.02 to 1.60 ± 0.02. The strongest absolute $N_d^{1/3}$ RMSE reductions (-0.25 to $-0.5\,\mathrm{cm}^{-1}$) are at the equator, where the prior N_d over the oceans might be therefore indicating differences in sulfate PSD in regions dominated either by oceanic or anthropogenic emissions. If this is the case, it might be beneficial to introduce an additional aerosol mode, either for sulfates or internally-mixed aerosol, to more precisely represent the spectrum of sulfates PSDs. Optimal PSDs for nitrate and organics CCNs (see Table 4) are systematically shifted toward larger particle sizes relative to the prior definitions, respectively resulting in number reduction by factors 0.36 and 0.19. Such results for organics are due to OM aerosols at cloud level peaking over sub-Saharan Africa , Northern India, China and South-East Asia (not shown), which are all regions where have a strong positive bias associated with OM-dominated CCN over Central Africa (RDND $\gtrapprox 0.50$), and at latitudes larger than 30°S, where model N_d tends to be overpredicted using the default definitions. Sare negatively biased (RDND $\lessapprox -0.50$). However, simulated moderate (RDND up to ≈ 0.2) residual bias patterns persist throughout the tropics and at latitudes south of 45°S (see Figure 3). Subtropical open-sea regions are also visibly degraded after the optimisation (RDND from ≈ 0.05 to ≈ 0.15). Also, the low N_d are degraded over sub-Saharan Africa and the tropical South Atlantic Ocean in the optimized setup. These results reflect the frequent co-presence of sulfates, soot and nitrates CCN whenever there are organics, so that simultaneous optimization might result in local degradation in order to improve the global metric. We are aware that the IFS wet scavenging scheme might be underestimating the aerosol mass fraction scavenged by precipitation in liquid clouds, which may result in overestimated aerosol mass concentrations and, in turn, simulated N_d. This is due to the fact that the fixed scavenging coefficients (between 0.7 and 0.9) for hydrophilic species are significantly lower than the typical mass activation rates close to unity provided by the activation scheme. We quantified the relative change in aerosol mass burdens obtained by diagnosing the scavenging coefficients from the activation scheme lies within 5% for SS and AM, within 15% for SU, NI, SOA and SOB, and within 18% for OM (more details are given in Appendix C). Errors in simulated aerosol burdens for these species are therefore unable to explain the generally-low N_d values prior to tuning, and insufficient to address the large overestimation over tropical Africa. Moreover, producing the required number by scaling mass would linearly impact AOD, which would be directly observable, especially at tropical latitudes, where the model rarely overestimates AOD, especially over sea (see discussion below) . We selected six bias over Australia worsens after optimisation (RDND from ≈ -0.15 to ≈ -0.3) as a result of the reduction of J for Org species.

We selected eight regions to better investigate remaining errors after the optimization procedure: over the north tropical Pacific (NTP), southern equatorial Atlantic (SET), biases after the optimisation procedure: north tropical Africa (NTA), central Africa (CAF), mid-Atlantic (MAT), central Africa (CAF), north tropical Pacific (NTP), Southern Indian Ocean (SIO), Southern Pacific (SOP), Europe (EUR) and India (IND). Their extents are reported in Table 3 and illustrated in Figure 4. All defined regions except Europe are characterized by Figure 3 shows that NTA, MAT, CAF, NTP regions all suffer from a high N_d bias ranging from 15% (NTP)to more than 60% in relative $N_d^{1/3}$ difference (see Figure 3). The mean simulated and observed monthly $N_d^{1/3}$ for a seleciton of regionsare illustrated residual bias relative to $N_{d,\mathrm{Q06}}$ after the InCloud optimisation (RDND between ≈ 0.15 and ≈ 0.30), while SIO and SOP regions are biased low ($-0.15 \gtrapprox \mathrm{RDND} \gtrapprox 0$). For these two groups of regions, monthly observed and simulated N_d are illustrated as spider plots in Figure 5; these include the NTA, CAF and MAT regions of overestimation, as well as the NTP , SOP and SIO regions, where the optimization procedure had a neutral to decisively positive impact. For the NTP region , simulated N_d for . In the case of the NTP region both prior and optimized setup optimised model N_d are within the uncertainty range spanned by of the observations, with the prior located at the lower end and the optimized values at the upper end; the residual difference between the while for the SIO and SOP regions, despite a significant increase in simulated N_d values and those provided by the tuning target is large (up to 20%) in terms of instantaneous impact on cloud reflectivity. Such large impact is due both to the relatively-clean conditions of the NTP region and the magnitude of the after optimisation, these remain below the lower end of the uncertainty range, loosening the constraint for the representation of the Twomey effect in this region. For typically found at $\approx 60\ \mathrm{cm}^{-3}$. Finally, in the NTA, CAF and SEA regionsinstead, the positive bias is located out MAT and CAF regions, the prior simulated N_d exceeds the upper bound of the uncertainty bars and has a rather strong seasonality: the bias peaks during the period November-March for the NTAregion, December-February and June-September for the CAFregion, August-October for the SEA region. The aerosol speciation for range with a clear seasonal pattern: December–February for NTA, December-March and June–September for CAF, July–October for MAT. After optimisation, N_d values fall within the uncertainty range in all three regions, but tend to remain near the upper bound and biased high with respect to $N_{d,\mathrm{Q06}}$ (Figure 5) during these periods. Aerosol speciation in these three regions indicate that between indicates that 60%and 90–90% of simulated N_d values are due to activation of organics and soot CCN originates from OM and BC particles (not shown). In the IFS-COMPO, carbonaceous aerosols emissions from observed wildfires are represented via the Global Fire Assimilation System (GFAS), that provides daily inventories of emissions by assimilating fire radiant power from satellite observations (Kaiser et al., 2012). Figure 13 shows that, for the CAF and NTA regions, wildfire carbon-containing aerosol emissions from GFAS are a very good predictor of errors in simulated , which are typically associated with wildfires.

5.2 N_d without black carbon (InCloudNoBC)

If BC is excluded from the CCN calculations, the resulting optimal aerosol PSDs produce effects qualitatively in line with InCloud, but with a significantly weaker reduction for Nit ($\times 0.93$) and Org ($\times 0.31$) CCN species (Table 4). For this setup, optimal PSDs for all species except fine sea salt (Ssf) are closer to the prior PSDs than for InCloud (Table 4). At the end of the InCloudNoBC optimisation $\mathcal{L} = 1.62 \pm 0.03$, so that the final result is not significantly different from InCloud ($\mathcal{L} = 1.60 \pm 0.02$).

CCN provider	prior	InCloud	ClBase3	InCloudNoBC
	$r_{\rm med}$	$r_{\rm med}\{r_{\rm med}^{0.1}, r_{\rm med}^{0.9}\}$	$r_{\rm med}\{r_{\rm med}^{0.1}, r_{\rm med}^{0.9}\}$	$r_{\rm med}\{r_{\rm med}^{0.1}, r_{\rm med}^{0.9}\}$
	[µm]	[µm] (num. ratio)	[µm] (num. ratio)	[µm] (num. ratio)
sulfate (Sul)	0.1100	0.106 {0.100, 0.110} (1.11)	0.144 {0.134, 0.153} (0.44)	0.109 {0.104, 0.114} (1.03)
nitrate (Nit)	0.0355	0.040 {0.038, 0.041} (0.69)	0.044 {0.042, 0.045} (0.52)	0.036 {0.036, 0.038} (0.93)
sea salt fine (Ssf)	0.1000	0.063 {0.062, 0.064} (3.96)	0.073 {0.073, 0.074} (2.55)	0.063 {0.061, 0.064} (4.03)
organic (Org)	0.0900	0.208 {0.171, 0.249} (0.08)	0.167 {0.158, 0.181} (0.16)	0.133 {0.122, 0.142} (0.31)
soot (Soo)	0.0118	0.010 {0.010, 0.010} (1.56)	0.011 {0.011, 0.012} (1.11)	—

Table 4. Optimisation results summary for each CCN-providing species (see Table 2) and each of the three optimisation setups described in the text. Reported are prior and optimised PSD median radii $r_{\rm med}$, 0.1 and 0.9 quantiles $r_{\rm med}^{0.1}$ and $r_{\rm med}^{0.9}$ and the implied number ratio $J_{\rm optimised}/J_{\rm prior}$. For sea salt coarse (Ssc), $r_{\rm med,ssc} = 10\, r_{\rm med,Ssf}$, therefore the number ratio is identical to Ssf.

Similarly, we found no significant difference in RDND between the optimised InCloudNoBC and InCloud N_d values on a monthly basis, respectively with a normalized covariance of 0.77 and 0.88, which narrows down our investigation to the regional wildfire seasons in Africa. The scatter plots report also the examples of the IND and EUR regions, where wildfires are instead a rather weak predictor of (not shown).

5.3 N_d from below cloud-base aerosol (ClBase3)

If N_d errors. However, to our knowledge, GFAS wildfire emissions in the NTA and CAF regions are unlikely to suffer from so strong a positive bias able to explain a four- to five-fold error in simulated are diagnosed from aerosols located three model levels below cloud base, optimal PSDs provide a strongly reduced J for Sul ($\times 0.44$), Nit ($\times 0.52$) and Org ($\times 0.16$), and higher J for Ssf ($\times 2.55$) (see Table 4). For all species except Ssf, the optimal $r_{\rm med}$ are significantly larger than for the InCloud setup. For the optimised ClBase3 setup, $\mathcal{L} = 1.38 \pm 0.03$; this setup is markedly better than InCloud at matching MODIS N_d as illustrated in due to the lower $N_d^{1/3}$ RMSE (Figure 3) at latitudes higher than 30°S over the ocean, where $|\mathrm{RDND}| \lessapprox 0.15$.

5.4 Consistency of optimal PSDs with aerosol optics

Figure 6 shows that the optimised (InCloud) PSDs for the group of aerosols including SS and NI tend to slightly increase AOD, with a larger relative impact at mid- to high latitudes in the Southern hemisphere, while the low-latitude signal is dominated by the reduced AOD from the group of OM, SOA, SOB aerosols. Overall, the mean and local impact (not shown) on total visible AOD remains typically within a 15%, partly also due to a compensation between the two aerosol groups. The increase in SS AOD at latitudes higher than 30°S provides the largest relative change on total AOD, which improves the DJF season and degrades the JJA season.

The change in AE due to the optimised (InCloud) PSD definitions is dominated ($> 90\%$) by the SS2 and SS3 aerosol (not shown). This is detrimental at the latitudes above 45° in the Summer hemisphere, where the model tends to be biased low, but

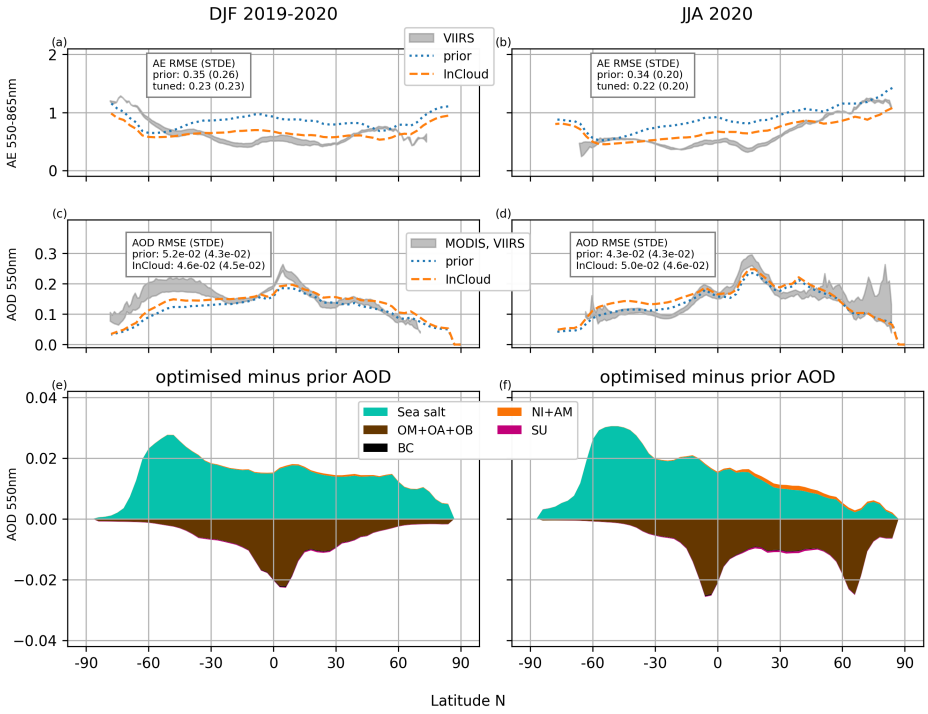

Figure 6. Simulated aerosol optical properties over the ocean for the DJF 2019-2020 (a, c, e) and JJA 2020 (b, d, f) seasons from Mie computations using the prior IFS aerosol definitions from Table 1 (prior), and using the median radii resulting from the InCloud N_d optimisation setup from Table 4 (optimised). Panels (a, b) show the zonal mean Angstrom exponent (AE) (550–865 nm), (c, d) zonal mean 550 nm AOD. Global RMSE in space for the seasonal mean values of simulated AE and AOD is also reported. The grey shadings display the range of observed zonal mean values from VIIRS (NOAA20 and SNPP) for the AE, and including also MODIS (Aqua and Terra) for the AOD. The bottom panels (e, f) show the optimised-minus-prior difference in AOD as a breakdown for the aerosol species used during the optimisation procedure.

mostly beneficial everywhere else. As a result, the global AE RMSE is reduced by more than 34% for both seasons (see Figure 6).

Figure 5. Figure 7 shows aerosol size spectra as observed by AERONET and simulated from CAMS aerosols for sites located close to the NTA and CAF regions. The plotted quantity is the PSD of the total spherical geometrical cross-section:

$$\frac{\mathrm{d}\sigma}{\mathrm{d}\ln r} = \pi r^2 \, r \frac{\mathrm{d}N}{\mathrm{d}r} \tag{10}$$

weighted by the Mie extinction efficiency $Q_{\mathrm{eff}}(r)$ $Q_{\mathrm{ext}}(r)$ at 550 nm for a real refractive index $m = 1.3$. By doing this, the area below the curves is an indicator of the optical depth of the entire aerosol column obtainable from such spectra. The flattening spectrum at particle radii smaller than $\approx 0.1\,\mu\mathrm{m}$ is due to the r^6 dependency of the extinction efficiency in the Rayleigh scattering regime. While these finer particles are the largest contributors to CCN numbers, they are the least detected from sun photometers, which poses an important limitation to using AERONET size spectra to validate CCN. 1.3. Selected

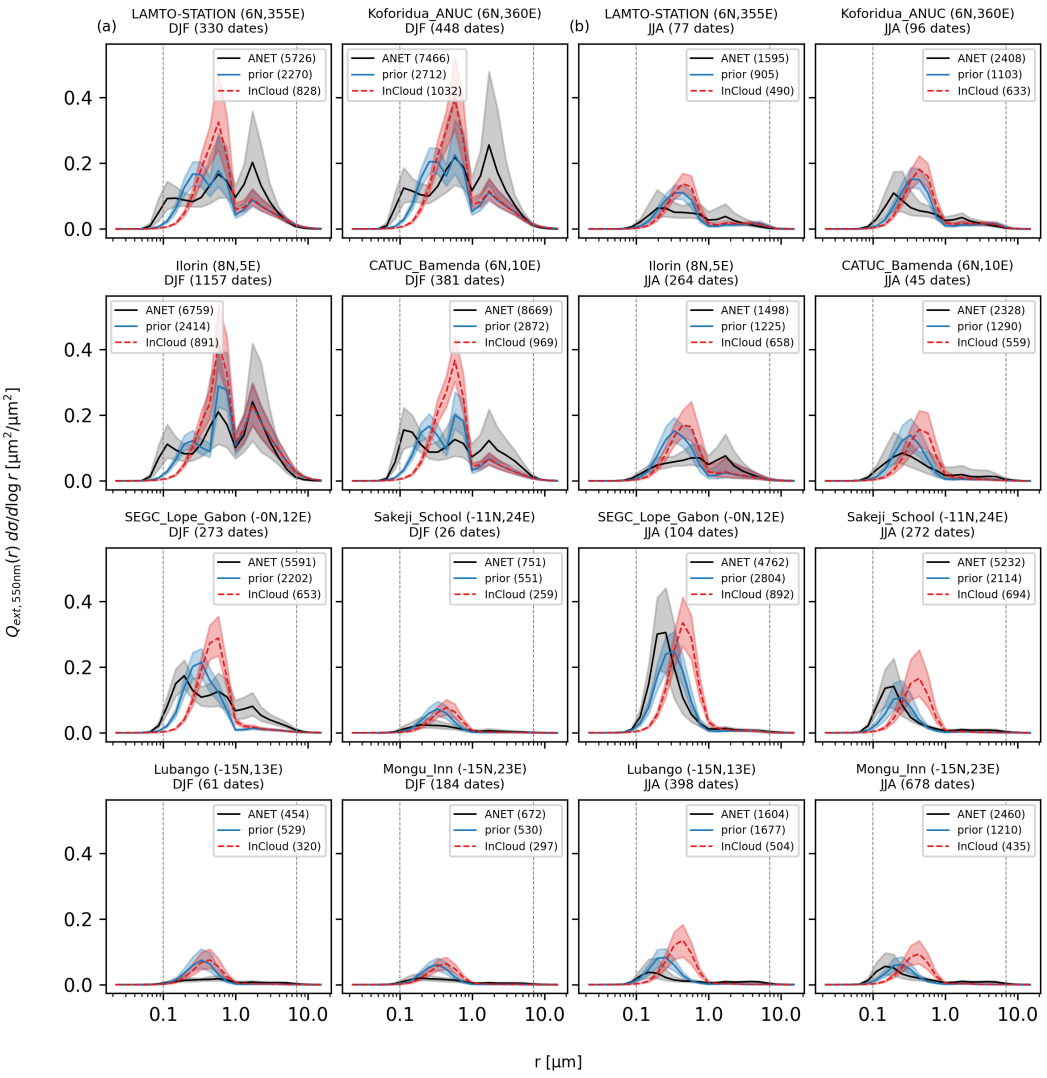

Figure 7. Aerosol size spectra (see Equation 10) for several low-latitude AERONET sites during the DJF (panel group a) and JJA (panel group b) seasons. The distribution is represented in terms of the spherical geometric cross-section (σ, see Equation 10) weighted by the Mie extinction efficiency at $550\ \mathrm{nm}$ for a real refractive index 1.3. Sites are ordered from top to bottom by decreasing latitude. AERONET spectra (ANET) are from all available observation dates, with total number of dates reported after the season label, and the corresponding IFS spectra are computed offline from experimental outputs for the seasons DJF2023-24 and JJA 2024, using both the 'prior' and 'InCloud' (optimised) PSD definitions (see Table 4). After each label are reported total column particle number concentrations calculated over the domain $[0.1\,\mu\mathrm{m}, 0.7\,\mu\mathrm{m}]$, with unit $10^{-3}\ \mu\mathrm{m}^{-2}$ (indicated by the dashed vertical lines), interpretable as the mean number concentration expressed in cm^{-3} for a $1\ \mathrm{km}$-deep layer with the same total-column amount of particles.

stations north and south of the equator present a peak in AOD respectively during the DJF and JJA season, consistentlywith the regional wildfire season. The most articulated Multimodal size spectra are found for the stations north of the equator, where three modal peaks are found: at 0.1 µm, 0.6 µm and 2 µmwith peaks at ≈ 0.1 µm, ≈ 0.6 µm and ≈ 2 µm. The two coarser peaks are also present in simulated values and are produced by Mineral Dust mineral dust likely advected by Northerly trade wind systems such as the Harmattan in from Western Africa. Interestingly, the finest The finest mode peak produced by the model is found around 0.3 µm (associated to at ≈ 0.3 µm (associated with OM aerosol), while it is located at less than 0.2 µm or even 0.1 µm in the AERONET data. Despite the overall typical number of particles being generally underestimated by the model, the overall area below the graph in the $r < 1$ µm regime is in fairly good agreement between model (prior) and observations. It is not straightforward to infer how shifting the carbonaceous aerosol population toward (finer) observed modes would impact simulated N_d. In fact, particles with radii < 15 nm are weakly activated into cloud droplets, especially when characterized by low hygroscopicity, as in the case of soot. By representing BC with the same PSD as pristine soot, the activation scheme might be overestimating the number of available BC particles. In fact, this setup implicitly neglects the property of soot to form large chain-like clusters, which results in a reduction of the effective number of separate particles available for activation. At the same time, the representation used in the activation scheme is expected to induce underestimated black carbon activated mass fraction by neglecting the property of such clusters to grow into larger structures and incorporate highly hydrophilic salt crystals like sulfates. Despite this uncertain representation, adding BC to the tuning procedure has a neutral-to-positive impact on results. For carbon CCN defined as in Table 2, we assessed a median simulated number activation rate around 0.5%. If we considered "realistic" aged BC in the form of aggregates of hundreds to thousands monomers oftentimes incorporating organics and sulfates crystals, this would imply a total amount of aggregates which is lower by two to three orders of magnitude, but which readily activate due to internal mixing with larger and more hydrophilic particles. This means that the total number of activated nuclei from BC particles would not be too far from the one simulated with the current setup. Therefore, even if for the wrong reason, the activation scheme might be providing fairly-realistic orders of magnitude for activated aged BC CCN. However, it is unclear whether this is enough to catch the variability in particle shape and size of real carbonaceous particles. Conversely, if we consider the possibility that the PSD for hydrophobic BC overestimates dispersion and/or the median particle size, this would result in an underestimation of the total amount of particles in the $r < 0.1$ µm regime, which would in principle explain the discrepancies in the size spectra in Figure 7. It is also key for the model to accurately simulate the emission category of carbonaceous aerosol, either soot or other organic compounds, as well as the conversion timescales from hydrophobic (pristine) to hydrophilic (aged) BC. Possible sources of error are a misrepresentation of the wildfire type (Forkel et al., 2025) and the associated smoke plume, with repercussions on the vertical aerosolprofile and efficiency of ageing processes.

5.5 Missing high-latitude CCNs

Very few fine sea salt particles are found at cloud level in our simulations. Figure 14 (a) shows that, during the optimization procedure, these play an overall negligible role as CCN providers, especially in high-latitude, stormy, open ocean regions regularly covered by boundary-layer stratocumulus clouds like the Southern Ocean. At lower latitudes, mixing of sea-salt transport

across boundary layer is facilitated by convective updraughts resulting in somewhat higher values at cloud level. In principle, low numbers concentrations agree with the understanding that sea-spray is typically a provider of CCN of secondary importance (e.g. McFarquhar et al., 2021); however coarse sea salt components are known to compete during activation with less hygroscopic particles (Fossum et al., 2020), impacting cloud optical thickness inversely to their concentration. Realistic aerosol profiles are therefore key to quantify such deactivation effect in the model. Our setup also displays negligible suppression effect (within 3% in relative τ change, not shown), mostly indicating absence of coarse sea salt particles at cloud level. Figure 14 a) shows that less than $30\,\mathrm{cm}^{-3}$ sea salt particles are found at mid- and higher latitudes at the cloud representative level during the tuning procedure. In many of these regions, like the Southern Ocean (SO), mixing is mostly driven by stormy weather. Multiple aircraft and ship campaigns observed SO clouds to be oftentimes in a mixed phase of super-cooled liquid water and ice crystals (McFarquhar et al., 2021). Figure 3 b) shows that diagnosing aerosols below cloud base, instead of inside the cloud, results in significantly higher numbers at mid- and high latitudes. This approach relies on the assumption that the cloud and the underlying boundary layer are well mixed, which is reasonable for stratocumulus clouds. This improves the output of the optimization procedure especially over the Southern Ocean (see figure 3 c, d) reducing the value of the loss function (see equation 7) at the end of the tuning for all the 18y period by 13%. From this result, we drew three main messages: firstly, sea salt profiles indicate weakly-superposing boundary layers between clouds and aerosols, with these latter sharply skewed toward the below-cloud space; secondly, such in-cloud values are so low that the tuning procedure is unable to retrieve the beneficial signal found instead below cloud base, indicating a very strong reduction of aerosols inside the cloud; thirdly, the too-low simulated N_d can potentially be tracked down to scarcity of CCN at cloud level. Using the optimised (InCloud) PSDs definitions (see Table 4) produces a modest shift in the size spectra of the finest peak, which is associated with OM aerosol, toward larger values, resulting in visibly degraded size spectra and deepening the low aerosol number bias against AERONET.

6 Testing changes in the aerosol wet-scavenging scheme

In order to investigate the low CCNconcentrations at cloud level we The results presented in Section 5 reveal a pattern of low biases at mid- to high latitudes (above 60°N and 45°S), that persist at the end of the optimisation. In these regions, aerosol concentrations tend to decrease sharply in the in-cloud relative to the below-cloud environment, typically coinciding with precipitating mixed-phase clouds. This motivated some targeted sensitivity tests with online experiments to explore the relevance of the wet removal of aerosols on the availability of simulated CCN.

We initially collected diagnostics of in-cloud (rain-out, IN-SCAV) and below-cloud (wash-out, BC-SCAV) wet scavenging (SC) as well as the release by precipitation evaporation (EVAP). These confirmed our expectation that IN-SC confirm the expectation that IN-SCAV from large-scale precipitation dominates the removal of SU and SS, while EVAPis significant in modulating tropical and subtropical aerosol mass budgets. For latitudes larger than 55° and along the intertropical convergence zone (ITCZ) the residence time due to IN-SC of an we found residence times due to IN-SCAV below one day for the entire column of SS particles is estimated around (10 hours, for SU is around) and SU (18 hours(not shown), impacts on total budgets for hydrophilic species on time scales below 1 day. Then, we performed a short (2 days) sensitivity experiment with switched off IN-SC for SS, yielding homogeneously distributed aerosols between cloud base and top (not shown). While this setup improved profiles, it also obviously results in non-realistically high concentrations overall, due to the impossibility to remove SS from the atmosphere. We decided to focus on the IN-SC parametrization).

We focused on the representation of the IN-SCAV parametrisation for precipitating mixed-phase (MP) clouds, where supercooled liquid and ice water coexist at temperature characterised by temperatures between $-38\ ^{\circ}\mathrm{C}$ and $0\ ^{\circ}\mathrm{C}$. For these clouds, the air is overall supersaturated with respect to ice but sub-saturated with respect to water and ice crystal growth occurs through the Wegener-Bergeron-Findeisen (WBF) process by deposition of water vapor while cloud droplets evaporate (Pruppacher and Klett, 2010). From the standpoint of aerosols, this implies evaporation of activated CCN into interstitial cloud space, therefore limiting the efficiency of aerosol removal by precipitation compared to warm-phase clouds, where only liquid water is present (Verheggen et al., 2007). Released aerosols incorporate information on micro-physical cloud processes occurred prior to evaporation, collection, collision-coalescence or nucleation, and are expected to be internal mixtures with size generally larger than the originally activated CCN particles (Hoose et al., 2008). Within the IFS single-moment cloud scheme no memory of cloud particle numbers is preserved, necessarily limiting the realism of a representation of the impact of the WBF process on aerosol number concentrationsand coexistence of supercooled liquid water and ice. Under these conditions, the IFS IN-SCAV scheme diagnoses aerosol removal rates by separately relating snow and rain formation respectively to ice and liquid cloud condensate. Aerosol scavenged mass fraction from snow is then modulated by a factor $\zeta \in [0,1]$, which is provided by the temperature-dependent parametrisation from Verheggen et al. (2007), so that $\zeta(T)$. Based on observations at one station in the Swiss alps, Verheggen et al. (2007) produced two parametrization to modulate activation efficiency in mixed-phase clouds. The first one defines a modulating factor function of cloud temperature, here referred to as $\zeta(T) \in [0,1]$, to scale the activated number fraction of aerosol particles with diameter larger than $100\ \mathrm{nm}$; the second one defines the same modulating factor but as the same observational dataset, Verheggen et al. (2007) also proposed an alternative parametrisation as a function of the cloud ice water

ratio $IWR \equiv IWC/(IWC + LWC)$, $\zeta(IWR)$. The same parametrization has $\mathrm{IWR} = \mathrm{IWC}/(\mathrm{IWC} + \mathrm{LWC})$, $\zeta(\mathrm{IWR})$, that has since been deployed in other global transport models leading in increased black carbon burdens at high latitudes that better matched observations from the HIPPO aircraft campaign (Liu and Matsui, 2021). The IFS IN-SC scheme diagnoses the aerosol removal rates by relating formation of snow to the cloud ice content and formation of rain to the cloud liquid content. Aerosol activated mass fraction is then scaled by $\zeta(T)$ whenever snow is produced (ECMWF, 2024a). several aerosol modelling studies (e.g. Hoose et al., 2008; Liu and Matsui, 2021).

We present here results about the two following experiments with modified IN-SC parametrization from two IN-SCAV parametrisation formulations modified in the following ways:

- **IWR2MOD1** uses $\zeta(\mathrm{IWR})$ to scale activated mass fraction both when either snow or rain is produced in mixed-phase conditions, rather than using $\zeta(T)$ only for snow;
- **IWR5MOD2** adds the following to the setup of IWR2: MOD1:
  - diagnose the aerosol removal rate using the ratio between the precipitation formation and the total cloud condensate instead of treating the ice and liquid phases separately;
  - $\zeta = 1$ at riming regimes regimes where riming prevails, identified with T between 261 K and 265 K when LWC $> 1\ \mathrm{g/m^3}$ following Qi et al. (2017);
  - set mass activation rates to 1 for all hydrophilic species except BC, consistently with numbers provided by the activation scheme;
  - balance opposite-sign formation rates of rain and snow to exclude freezing and melting from the IN-SC routine;
  - implement a bug-fix for overestimated sedimentation of medium and coarse sea-salt dry deposition. Figure 8 shows LWC $> 1\ \mathrm{g/m^3}$ following Qi et al. (2017).

6.1 Online IFS-COMPO experiments

To test the sensitivity of ACI to the wet removal of aerosols in mixed-phase clouds, we performed a series of online IFS-COMPO simulations. These use meteorological initial conditions from ERA5 analyses, while chemical and aerosol tracers are restored from the previous forecast day at valid time +24h, thus leaving them free to evolve. These runs have a resolution of $\approx 39\ \mathrm{km}$.

Figure 8 displays a cross-section of the model simulation output for a case-study on September 1718, 2024, using a 10-days spin-up time ; the of 10 days. We use aerosol number mixing ratios of CCN in (computed from prior CAMS PSDs), i.e. aerosol number concentration per unit mass of air, for Sulfate (SU), Sea Salt bin 1 (SS1) and Organic matter (OM) as an upper-bounding proxy ($\mathrm{CCN_{max}}$) for CCN concentrations. This case shows that for the control simulation drops to values below $30\ \mathrm{cm^{-3}}$ in high-latitude $\mathrm{CCN_{max}}$ drops to extremely low values (well below $10\ \mathrm{cm^{-3}}$) in mixed-phase clouds simulated over the SO forming snow precipitation consistently to what stated above about the sea salt CCN diagnostics in- and below the cloud. The IWR5 setup increases CCN numbers found inside the cloud up to about Southern Ocean. With the MOD2 version

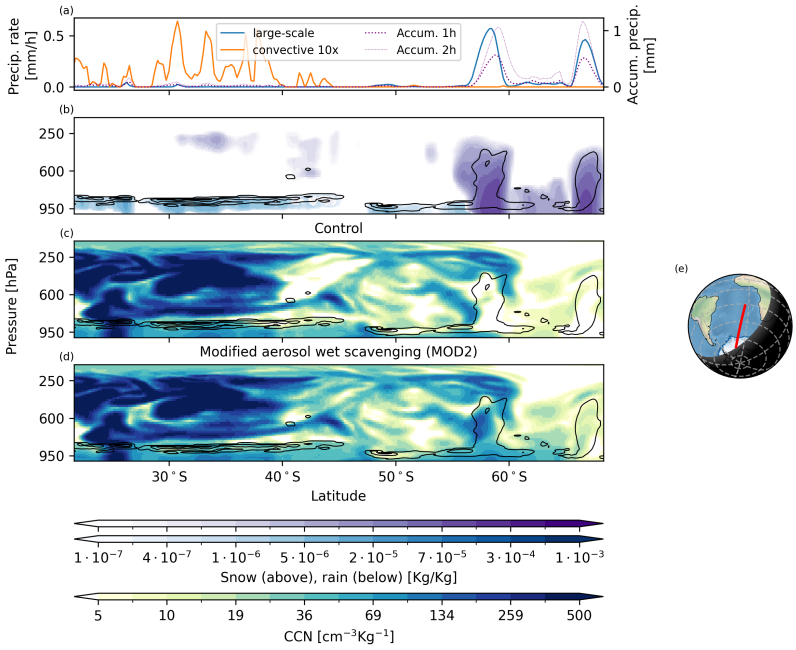

Figure 8. Cross-section of IFS-COMPO simulation (online) on 18 September 2024, 15:43 UTC. From top to bottom, total instantaneous large-scale and convective precipitation rates and accumulated total precipitation (1h, 2h) at the surface (a, note that instantaneous convective precipitation is multiplied by a factor 10 for visualisation purposes). Panel (b) shows the cross-section of instantaneous specific rain and snow water contents; panel (c) the cross-section of $\mathrm{CCN_{max}}$, defined as the number concentrations per unit mass from Sulfate (SU), Sea Salt bin 1 (SS1) and Organic Matter (OM) aerosol; panel (d) is the same as (c) but for the MOD2 simulations. Black contours in panels b-d are for total cloud water mixing ratio (first contour at $2 \cdot 10^{-5}$ and spacing by $5 \cdot 10^{-5}$). The track location on the globe is shown in panel (e).

of the model, $\mathrm{CCN_{max}}$ is significantly higher throughout the same ice-containing cloud profiles, with values up to $100\ \mathrm{cm^{-3}}$, providing a background of CCN compatible with higher and more realistic N_d values. . $\mathrm{CCN_{max}}$ is also increased at lower latitudes, where snow is present aloft, which is particularly evident at 42°S, between 650 hPa and 250 hPa.

We also tested the IWR2 and IWR5 setups by performing CAMS daily forecasts MOD1 and MOD2 by performing more extended simulations over the boreal winter (DJF) 2023-2024 and boreal summer (JJA) 2024 seasons. These simulations use meteorological initial conditions from ERA5 analyses, while chemical and aerosol tracers are restored from the previous forecast day at valid time +24h, thus leaving them free to evolve. These setups use a spin-up time of 1 month to ensure that tracers are aligned with the climate of the model. Figure 11 shows a comparison between column-integrated aerosol size spectra from the model and the corresponding AERONET inversion product Dubovik and King (2000) for the stations at the highest latitudes in the southern (DJF season) For these cases, the "Control" experiment uses the default IFS CY49R1, where N_d do not depend on aerosols, "InCloud" diagnoses N_d from aerosols (ACI) at cloud level using the InCloud optimal PSDs, while MOD1 and MOD2 experiments add the corresponding IN-SCAV modifications on top.

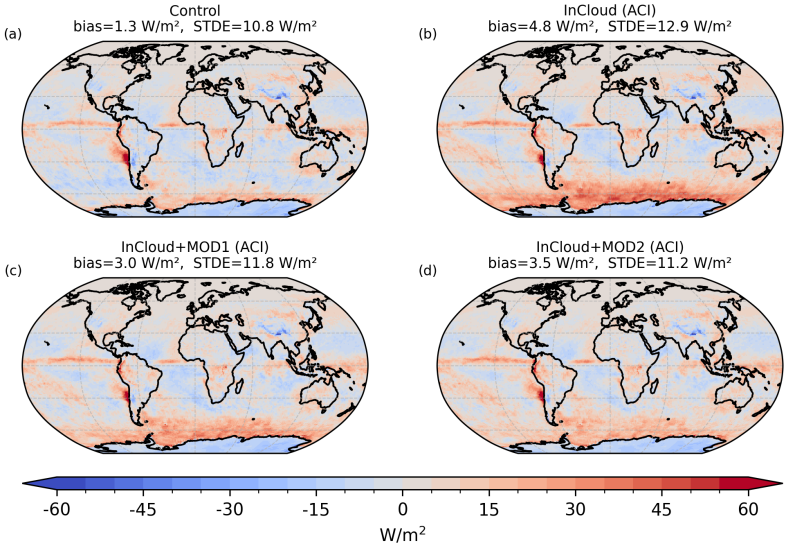

Figure 9. Mean top-of-atmosphere (TOA) shortwave (SW) radiation flux (outgoing), difference of CERES minus IFS for the season DJF 2023-2024, with global bias and STDE on monthly means for each experiment. For the control (a) N_d does not depend on aerosols; for b), c) and d) N_d is diagnosed from aerosols (label ACI) using optimal PSDs from the InCloud setup. These use the default IFS IN-SCAV configuration (b), MOD1 (c) and MOD2 (d). Details are provided in the text.

6.2 TOA SW flux diagnostics

Figure 9 shows the top of the atmosphere (TOA) biases in simulated SW fluxes against CERES for the DJF 2023-2024 season experiments. The InCloud (ACI) experiment has both larger absolute bias ($+3.5\ \mathrm{W\,m^{-2}}$) and error standard deviation (STDE, $+2.1\ \mathrm{W\,m^{-2}}$) than Control. The strongest contribution to this degradation is over the Southern Ocean, where TOA SW biases are increased by $\approx 20\ \mathrm{W\,m^{-2}}$ in the sense of reduced cloud albedo. With the InCloud-MOD1 and northern (JJA season) hemisphere. The same figure reports total column numbers obtained by integrating $\frac{\mathrm{d}N}{\mathrm{d}r}$ over the domain $r \in [0.1\ \mu\mathrm{m}, 5\ \mu\mathrm{m}]$. The reason for restricting the integration domain is in the progressively lower sensitivity and larger errors in the AERONET product towards the tails of the distribution as reported in (Dubovik and King, 2000). This constitutes an important limitation to the validation of aerosol number concentrations using measurements from sun-photometers: in fact, despite a large majority of particles are found at radii smaller than $0.1\ \mu\mathrm{m}$, these interact very weakly with visible wavelengths, due to a decline in extinction efficiency $Q(r) \propto r^6$ in the Rayleigh regime. For InCloud-MOD2 experiments, STDE is reduced respectively by $1.1\ \mathrm{W\,m^{-2}}$ and $1.7\ \mathrm{W\,m^{-2}}$ compared to InCloud, with a mean increase in reflected SW radiation over the Southern Ocean up to $\approx 20\ \mathrm{W\,m^{-2}}$.

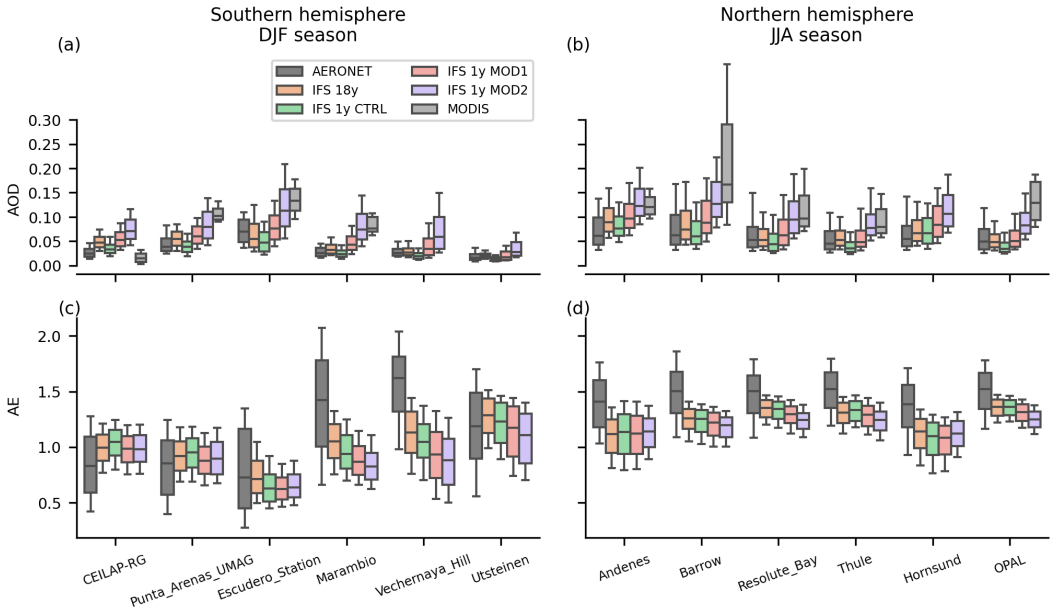

Figure 10. Boxplots of AOD (a, b) and Angstrom exponent (AE) (c, d) for high-latitude AERONET sites in the southern (a, c) and northern (b, d) hemisphere, as in Figure 11. AERONET and MODIS (Aqua and Terra means) data cover the period 2003–2020. MODIS values are shown in panels (a, b) only where at least 10 months of valid retrievals are available. AERONET means are based on a limited number of valid daily observations, typically between 200–800 days per site, with substantially fewer observations for the Escudero site (47 days). The simulated values labelled 'IFS 1y' refer to the 1-year simulation for the Control (CTRL), MOD1 and MOD2 setups. To facilitate the comparison across the different periods of observational and simulation coverage, simulated values based on the stored aerosol fields used for the optimisation, covering 2003–2020 ('IFS 18y'), are also shown.

6.3 AOD, AE and aerosol size spectra

We evaluate mean experiment outputs using mean observations of all available AERONET $550\,\mathrm{nm}$ AOD, $440-870\,\mathrm{nm}$ AE and size spectra over the period 2004-2024 at several high-latitude stations, six for each hemisphere. These are shown in Figure 10 and cover the summer season (DJF for the southern and JJA for the northern hemisphere).

Figure 10 shows AOD and AE boxplots for the selected AERONET stations. The control simulation has comparable $550\,\mathrm{nm}$ AOD with respect to AERONET, but tends to be biased low with respect to the co-located MODIS AOD for most sites with enough valid retrievals. The model also tends to produce systematically low-biased AE (up to ≈ -0.8) against AERONET, but this difference is only occasionally larger than the joint model-observations interquartile range. The MOD1 and MOD2 simulations result in generally increased AOD (up to $+0.05$) and decreased AE (up to -0.5) for all locations, which represent a degradation with respect to mean AERONET observations.

Figure 11 shows the total-column AERONET and model size spectra (expressed as weighted cross-section size distributions, see Equation 10) during the summer season at the selected high-latitude stations. For each location are reported total column

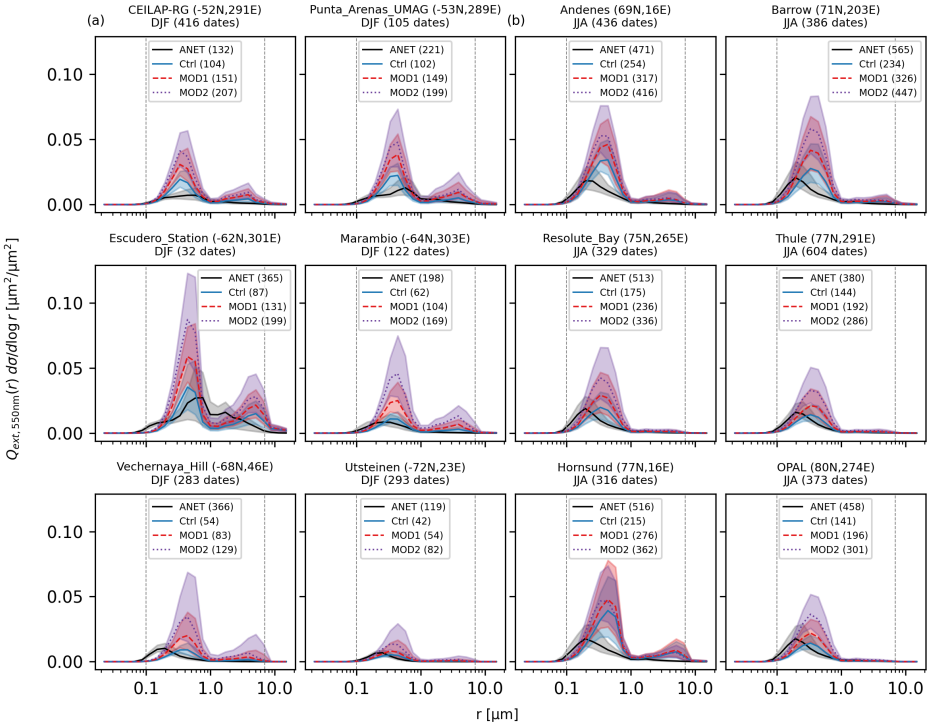

Figure 11. Aerosol size spectra at a selection of high-latitude AERONET locations, respectively for the southern (group a, season DJF) and northern (group b, season JJA) hemisphere. Like in Figure 7, spectra are represented using the spherical geometric cross-section (σ) weighted by the Mie extinction efficiency at $550\,\mathrm{nm}$ for a real refractive index 1.3. Sites are ordered from top to bottom by increasing (absolute) latitude. AERONET spectra (ANET) are from all available observation dates (total number after the season label), while the corresponding IFS spectra are calculated offline from experimental outputs for the seasons DJF2023-24 and JJA 2024 using the two changed mixed-phase clouds wet-scavenging parametrisations MOD1 and MOD2. After each label are reported total column particle number concentrations calculated over the domain $[0.1\,\mu\mathrm{m}, 7\,\mu\mathrm{m}]$ (indicated by the dashed vertical lines), with unit $10^{-3}\,\mu\mathrm{m}^{-2}$, interpretable as the mean number concentration expressed in cm^{-3} for a $1\,\mathrm{km}$-deep layer with the same total-column amount of particles.

number concentrations obtained by integrating $\frac{\mathrm{d}N}{\mathrm{d}r}$ over the domain $r \in [0.1\ \mu\mathrm{m}, 7\ \mu\mathrm{m}]$, over which the errors of the retrieved $\mathrm{d}V/\mathrm{d}\ln r$ are estimated within 10% (Dubovik and King, 2000). For all stations at latitudes higher than 60N and 60S the control 60°N and 60°S the Control simulation has lower particle counts within the integration domain, while IWR2 and IWR5 result in significantly increased particle numbers (with differences up to $300\ 10^{-3}\ \mu\mathrm{m}^2$), while MOD1 and MOD2 have significantly higher particle number concentrations than Control (factor 1.5 to 2) resulting in better agreements with values from AERONET . Figure 10 shows that , in terms of AOD, the control simulation agreement with AERONET (see numbers after each label in Figure 11). The size spectra illustrate that this is associated with an increased aerosol mode centred around $0.3\ \mu\mathrm{m}$ which tends to be biased high with respect to AERONET . The model also tends to produce systematically low AE values, which points at an overestimate of AOD contribution from coarse aerosols. coarser and with larger amplitude than the finest AERONET mode (around $0.15\ \mu\mathrm{m}$). This pattern holds consistently for all stations except CEILAP-RG (Argentina), which is the lowest-latitude (52°S) location of the whole set.

The optical thickness in the simulated spectra is provided by modes shifted to larger sizes compared with AERONET; these larger modes are also amplified in IWR2 and IWR5 MOD1 and MOD2 that, despite providing better agreement in particle numbersnumber concentrations, tend to be biased high in AOD against AERONET. It must be noted that this contrasts with validation against satellite AOD. In fact, Figure 10 shows that at high latitudes the model's AOD tends to be biased low compared to MODIS, and biased high compared to AERONET. Such discrepancy between MODIS and AERONET AOD at high latitudes is seems consistent with the analysis reported in Gupta et al. (2018). The IWR2 and IWR5 by Gupta et al. (2018), but this case also shows that a more accurate quantification of biases of AOD from satellite at relatively high latitudes (above 60°) would give significant insights for systems like CAMS operationally assimilating global observations of AOD from satellites. The MOD1 and MOD2 experiments have systematically higher AOD at high latitudes, but tend to have systematically lower AE than AERONET, which indicates too large a contribution to AOD by coarse mode aerosols. Better understanding of such discrepancies is limited by These discrepancies are however difficult to interpret due to the relative scarcity of observations from sun photometers at high latitudes especially in the Southern Hemisphere, and the as well as the almost complete absence of observations over sea. Figure 9 shows the top of the atmosphere (TOA) biases in SW fluxes against CERES for the DJF 2023-2024 season. The panels show results of a control simulation, where cloud N_d and r_e are computed by the IFS wind-dependent parametrization and three simulations where cloud N_d values are diagnosed from aerosol fields by the activation scheme, all labeled as "InCloud". Of the three InCloud simulations, one uses the default wet scavenging parametrization, the other two use the IWR2 and the IWR5 setup. Note that the all setups use the same aerosol PSD definitions resulting from the InCloud optimization discussed in section 5. Like many global models (Bodas-Salcedo et al., 2014), the IFS reflects too little SW radiation over the Southern Ocean, and this is consistently illustrated by the control simulation. InCloud displays a strong degradation by up to $20\ \mathrm{W/m^2}$ (see figure 9) of the TOA SW bias over the SO, associated with decreased optical thickness of clouds, consistently with the indication of too low N_d values at these latitudes. Such degradation is strongly reduced by InCloud-IWR2 and totally removed by InCloud-IWR5, which has an overall neutral impact over the SO. open sea regions.

As a final global evaluation of the sensitivity experiments, Figure 12 shows the zonal mean (only over sea) AOD evaluation of $550\ \mathrm{nm}$ AOD zonal mean and zonal RMSE against MODIS (M3 monthly) of the experimental setupsfor the experiments.

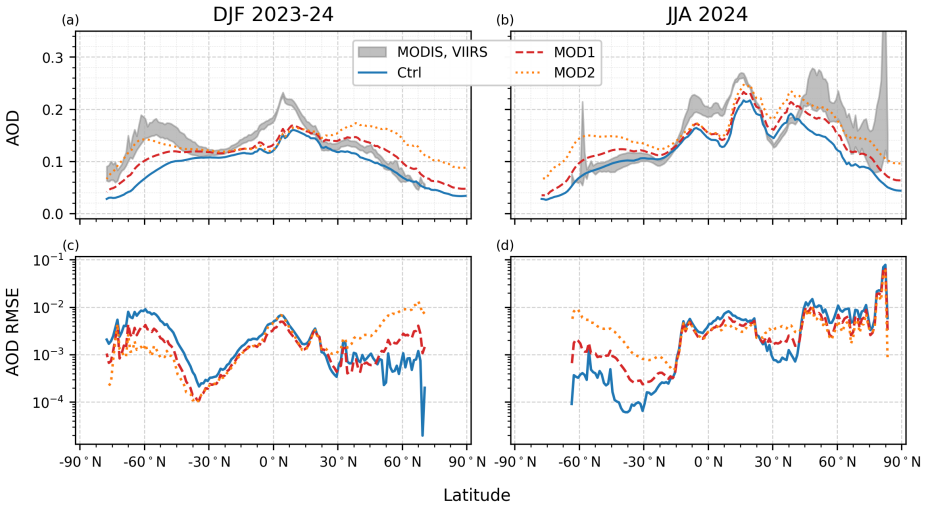

Figure 12. Zonal mean (a, b) and zonal RMSE (c, d) of seasonal 550 nm AOD during the DJF 2023-2024 season (a, c) and the JJA 2024 season (b, d). The grey shaded region is bounded by the AOD values calculated from MODIS and VIIRS, while the solid, dashed and dotted lines represent respectively the output of the control ('Ctrl') and the simulations with modified wet-scavenging MOD1 and MOD2. The RMSE is calculated with respect to the mean of the MODIS and VIIRS AOD values. We included only points over the ocean, where the MODIS pixel count for AOD was larger than 150 and VIIRS had at least 7 days of valid retrievals.

The largest absolute impact of IWR2 and IWR5 is found at the high latitudes toward increasing aerosol burdens; these coincide to regions where the tuning procedure struggled the most at producing large enough N_d values. Over the SO the two setups set a decisive improvement against MODIS, with biases being almost eliminated during the JJA season between latitudes 45S and 60S in the IWR5 setup. In the winter hemisphere , IWR2 and IWR5 seem to produce too large AOD at latitudes as low as 45N and 30S, indicating that the system might be lacking the right seasonal cycle of emissions over the oceans at high latitudes. A possible explanation could be that the IFS, despite linking SU production to the oxidation of available dimethyl sulfide (DMS), has no representation of sea-borne marine organic aerosols. These are likely linked to photosynthetic activity of phytoplanktons (Sellegri et al., 2024) and are found to significantly contribute to spatio-temporal variability of cloud N_d (McCoy et al., 2015). Therefore, considering sea spray as only SS containing might result in an overestimated burden of SS, with boundary layer aerosols lacking the correct seasonal cycle. MOD1 and MOD2 is at mid- and high latitudes towards increased aerosol burdens, with up to ≈ 0.05 increase for MOD2. This results in the zonal RMSE being significantly reduced for the summer hemisphere by up to ≈ -0.1, and increased by the same amount over the winter hemisphere.

7 Discussion

We open this section by discussing overall limitations and performance of the N_d optimisation, and the magnitude of observational biases relevant to the optimisation results. Next, we focus on two discussion streams: one concerns the tendency of the model (partially mitigated with optimisation) to simulate N_d biased toward the upper bound of the uncertainty range; the other deals with the systematically low N_d at mid- and higher latitudes in the Southern hemisphere, where the optimisation is unable to bring improvement, and how the outcome of the sensitivity tests compare with the optimisation results. In both cases, results from the different setups (InCloud, InCloudNoBC, ClBase3), combined with independent observations, are used to clarify to what extent each optimal PSD can be interpreted as physically plausible, and when it compensates for non-tuned aspects such as speciation, ageing or poor mass concentration representation.

7.1 Limitations and effectiveness of the N_d optimisation

While the magnitude of reduction of $\mathcal{L}$ by only 13% may raise doubts about the effectiveness of the optimisation, it actually indicates that the prior (CAMS default) PSDs yield N_d values already close to the optimisation target. The intrinsic limits of the optimisation lie in the prescribed spatial aerosol patterns from the model fields, and the restricted number of free parameters (the PSD r_{med} for five species). This is illustrated by the ClBase3 optimisation setup, where the prior N_d prediction has much larger errors throughout the tropics; in this setup, the improvement brought by the optimisation is significantly stronger, with a reduction of $\mathcal{L}$ by 21%.

The optimised (InCloud) PSD r_{med} for SU is close to the prior $0.11\,\mu\text{m}$, keeping the increase in particle number below 11% and the optical effect non-detectable. This PSD was independently updated in IFS-COMPO CY49R1 (from $r_{\text{med}} = 0.0355\,\mu\text{m}$ and $\sigma = 2.0$) and we found that using the old PSD led to significantly larger number concentrations of activated SU by up to a factor $\times 2.7$ (not shown), which the optimisation would then need to correct. While the new prior SU performs fairly well globally, observations of tropical marine sulfate aerosol have indicated mass transfer from Aitken ($r \approx 0.04\,\mu\text{m}$) to accumulation ($r \approx 0.1\,\mu\text{m}$) mode (Hoppel et al., 1990). However, the IFS-COMPO does not currently represent changes in aerosol PSDs over time, and in general no transfer of mass across bins is allowed (ECMWF, 2024a). Other models like the Met Office Unified Model do represent Aitken and accumulation modes for sulfate, and assess typical local mass ratios of 1:9 (Jones et al., 2001; Mulcahy et al., 2014). This variability in sulfate PSD is a possible explanation for the pattern of N_d magnitudes over the oceans, with high N_d biases over subsidence regions, and neutral-to-low in convective regions, indicating a potential benefit of an additional Aitken aerosol mode, either as sulfate or internally-mixed aerosol.

The fixed mass wet scavenging coefficients used by the IFS (between 0.7 and 0.9) for most hydrophilic species tend to be smaller than the typical mass activation rates close to unity provided by the activation scheme. Therefore, we performed an online IFS-COMPO simulation (setup as for simulations in Section 6) using scavenging rates diagnosed from the activation scheme and found the resulting changes in total aerosol mass to be within 5% for SS, SOA, SOB, within 10% for OM, and within 15% for SU and NI species (see Appendix C). For most species (SS, SU, AM, OM) the resulting reduced burdens would

tend to increase the prior N_d biases for the optimisation, while in the case of OM these reductions are too small to explain the reduction by a factor $\times 0.08$ to $\times 0.31$ required by the optimisation.

7.2 Biases attributable to the observations

MODIS N_d retrievals are known to suffer from an optical penetration bias due to the assumption that the spectrally-retrieved r_e values are representative of the droplet PSD at cloud top, leading to overestimated N_d (MODIS 2.1 µm) retrievals between 20% and 40% for marine clouds. Bias-correction of retrievals has been shown to occasionally improve agreement with in-situ measurement campaigns, but implications on N_d budgets are still unclear (Gryspeerdt et al., 2022b). This translates to an upper-bound effect of 12% in $N_d^{-1/3}$ over marine regions within 30° latitude.

At latitudes higher than 60°N and 45°S our method struggles to sufficiently increase N_d to match observations. MODIS cloud retrievals are known to suffer from viewing geometry errors with large satellite and solar zenith angles (Maddux et al., 2010; Grosvenor and Wood, 2014), potentially degrading high latitude observations. According to Gryspeerdt et al. (2022b), at latitudes higher than 60° such errors are positive, on average within 16 cm^{-3}, potentially significant over relatively pristine regions over the ocean, with typical retrieved N_d values between 75 cm^{-3} and 100 cm^{-3}. These effects are included in one of the sampling strategies (BR17) and contribute to the error bars that we assigned to the MODIS N_d observations.

7.3 The tropics

The optimisation results highlight that carbonaceous (OM, BC) aerosols are critical contributors to tropical model N_d and, as such, require a more detailed discussion of their representation. Particles with radii < 15 nm are weakly activated into cloud droplets, especially when characterised by low hygroscopicity, as in the case of soot. Representing BC with the same PSD as pristine soot might overestimate the number of particles, but underestimate their activation rates. This is because such an approach implicitly neglects the property of soot to form large chain-like clusters (Teng et al., 2019, e.g.), resulting in a reduction of the effective number of independent particles available for activation. At the same time, this approach cannot represent the growth of such clusters into larger structures incorporating SU or OM particles (Yu et al., 2019, e.g.), making them more efficient CCN providers. Sensitivity of the activation efficiency to updraft velocity is expected in such aerosol-rich regimes; this sensitivity reflects both the relevance of ongoing efforts to better characterise updraft variability in global models (e.g. Ahola et al., 2022) and the difficulty of applying alternative approaches in our offline framework. However, updraft velocity plays a secondary role compared to aerosol number in determining the N_d bias, therefore the discussion will focus on the aerosol-related processes.

For carbon CCN defined as in Table 2, the median simulated number activation rate is around 0.5%. If we considered realistically-aged BC in the form of aggregates of hundreds to thousands monomers often incorporating organics and sulfate crystals, this would imply a reduced total amount of aggregates by two to three orders of magnitude which, however, readily activate due to internal mixing with larger and more hydrophilic particles. Moreover, BC ageing is an open area of research, and future work is needed to better characterise the role and relevance of aged BC and its representation on CCN simulations.

Sensitivity calculations of simulated optical properties (AOD, AE, spectra) indicate that the optimal PSD for OM is likely compensating for non-tuned processes. In fact, the optimised (InCloud) PSD visibly degrades the shapes of the aerosol size spectra and worsens the low bias in total column number concentrations (Figure 7). The fact that InCloudNoBC produces N_d of similar quality, but with a neutral impact on aerosol optics, indicates that the compensated biases are related to the co-existence of BC and OM aerosol. Most of the aerosol counts from AERONET spectra are associated with the fine-mode part of the distribution ($r \lessapprox 0.15\,\mu\mathrm{m}$); for those, the optical detectability quickly decays due to the r^6 dependency of the extinction efficiency in the Rayleigh scattering regime, progressively limiting the sensitivity (Dubovik and King, 2000) of the retrieval for $r < 0.1\,\mu\mathrm{m}$, where the number contribution to CCN from fine particles increases. However, the substantially flatter tail of the model spectra is consistent with the above-discussed limitations in the representation of OM and BC ageing.

In the IFS-COMPO, carbonaceous aerosol emissions are controlled by satellite observations of wildfires (Kaiser et al., 2012) via the Global Fire Assimilation System (GFAS). As shown in Figure 13, wildfire carbon-containing aerosol emissions from GFAS correlate well with observed N_d in both regions (normalized covariance of 0.71 and 0.90) and the difference between observed and simulated N_d (normalized covariance of 0.85 and 0.72) for the NTA and CAF regions, mirroring the seasonal biases in model N_d of Figure 5. This does not hold for other regions like IND and EUR, where wildfires are instead a weak predictor of N_d. The seasonality of N_d over North-tropical and central Africa, and downstream over the mid-Atlantic can therefore be linked to wildfire simulations, opening the possibility of using these results to support validation of related processes under active development for the wildfire assimilation systems, such as representation of wildfire types (Forkel et al., 2025) and associated smoke plumes.

We tested the robustness of the optimisation by excluding BC from the CCN calculations (InCloudNoBC). The rationale behind this is that the externally-mixed CAMS aerosol representation for this species is unsuited for describing the process by which BC is mostly scavenged in aggregated form with other, more efficient, aerosol particles and that therefore its contribution to the overall number of CCN is neutral. Results of the optimisation for this setup excluding BC from the CCN (labelled InCloudNoBC) are reported in Table 4 and are significantly closer to the prior definitions in the case of Org and Nit CCN providers. The almost identical final value of $\mathcal{L}_{\text{InCloudNoBC}}$ to the InCloud setup indicates that excluding BC brings no significant change to the optimised N_d. Furthermore, the InCloudNoBC optimal PSD for OM has an almost completely neutral effect on simulated OM AOD, which makes it a preferred option for its consistency with the current optical definitions; such neutral impact can be also appreciated by visually comparing the typical mass extinction efficiency at $r_{\text{med}} = 0.09\,\mu\mathrm{m}$ and $r_{\text{med}} = 0.13\,\mu\mathrm{m}$ for OMH in Figure 1. Given the equivalence of the resulting N_d, the higher consistency with OM aerosol optics and the significantly smaller size of the required LUT, InCloudNoBC emerges as a preferable configuration until CAMS BC representation is further improved.

The AE and AOD signal from SS aerosol (Figure 12) strongly depends on the decision to keep the two SS PSD modes geometrically spaced by a factor 10 (see Table 1). The rigid displacement of the entire bimodal SS PSD towards smaller sizes during the optimisation is therefore driven by the number values associated with Ssf, for which the mass contributions from SS1 and SS2 are typically 70% and 30%. By design, Ssc provides extremely low CCN number concentrations (order of the unit over a background of dozens to hundreds cm^{-3}); moreover, its role in reducing the activation efficiency of smaller, less

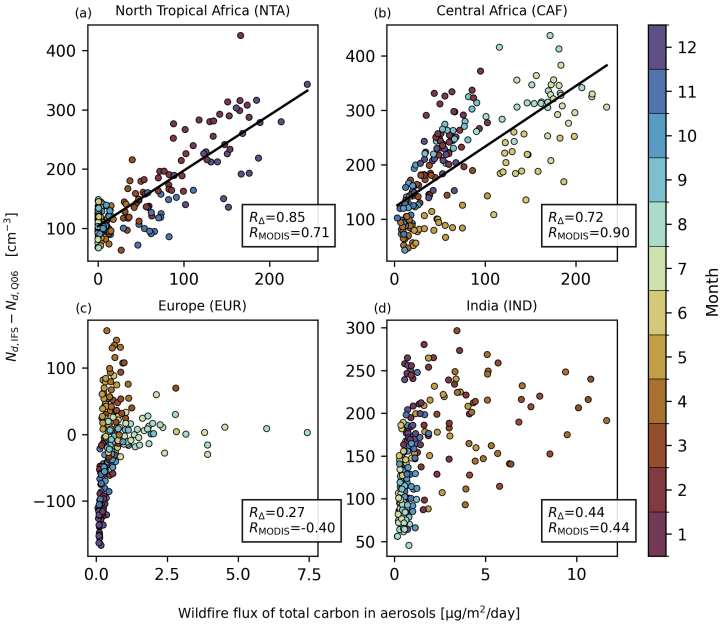

Figure 13. Scatter plot of wildfire flux of total carbon in aerosols (WFTCA) from the GFAS system and differences between simulated and MODIS 'Q06' monthly N_d (2003–2020). R_Δ and R_{MODIS} indicate the Pearson's correlation coefficients between WFTCA and respectively, the difference $\Delta = N_{d,\mathrm{IFS}} - N_{d,\mathrm{Q06}}$ (R_Δ), and $N_{d,\mathrm{Q06}}$ (R_{MODIS}).

hygroscopic particles, that we quantified within 15-20% in the subtropical stratocumuli (not shown), provides too weak a signal in the overall simulated N_d to allow independently constraining Ssc during the optimisation. However, the beneficial impact of decreasing AE over the ocean between 45°N and 45°S indicates that the current representation is plausibly underestimating the optical contribution of the coarse SS aerosol particles, and potentially also their relevance during aerosol activation.

7.4 The mid- and high latitudes

Testing the activation scheme (InCloud optimisation) with online IFS-COMPO experiments shows a widespread and strong decrease (up to $\approx 35\ \mathrm{W\,m^{-2}}$) of reflected solar radiation at latitudes south of 45°S, covering all the Southern Ocean (SO). Since the IFS, like many global models (Bodas-Salcedo et al., 2014), generally underestimates the amount of reflected solar radiation over the SO, this signal directly translates into a significant degradation of TOA SW fluxes. The understanding that these regions are strongly characterised by mixed-phase, boundary-layer cloud regimes (McFarquhar et al., 2021) motivated sensitivity tests targeting the aerosol wet removal for freezing clouds. For these clouds, air is typically supersaturated with respect to ice but sub-saturated with respect to water, so that ice crystal growth occurs via deposition of water vapour produced by evaporating cloud droplets, mechanism known as the Wegener-Bergeron-Findeisen (WBF) process (Pruppacher and Klett,

2010). From the standpoint of aerosols, this implies evaporation of activated CCN into interstitial cloud space, therefore limiting the efficiency of aerosol removal by precipitation compared to warm-phase clouds, where only liquid water is present.

Based on observations at one station in the Swiss Alps, Verheggen et al. (2007) produced two parametrisations to modulate scavenging efficiency in mixed-phase clouds, one temperature-dependent and the other phase-dependent, $\zeta(T)$ and $\zeta(\mathrm{IWR})$, to scale the activated number fraction of aerosol particles with diameter larger than $100\ \mathrm{nm}$. Since the IFS IN-SCAV scheme already applies $\zeta(T)$ to rescale the mass-scavenging rates whenever snow is produced (ECMWF, 2024a), we experimented two setups progressively adding complexity to the IN-SCAV scheme; the first by using a phase-dependent parametrisation of scavenging efficiency for both liquid and ice phase (MOD1); the second by explicitly treating mixed-phase conditions and riming processes (MOD2).

When evaluating global TOA SW biases, the MOD1 and MOD2 setups still increased STDE relative to control, but this degradation was significantly smaller than that of InCloud (default IN-SCAV scheme) respectively, by 52% (MOD1) and 86% (MOD2). In the MOD1 and MOD2 experiments relative to the standard InCloud setup, the SW flux change is dominated (more than 90%) by reduced cloud r_e because of higher diagnosed N_d by the activation scheme over the SO. This response is driven both by increased SS and SU aerosol burden (and associated AOD) at high latitudes, and by their longer persistence inside ice-precipitating clouds. Because no new optimisation was applied to MOD1 and MOD2 setups, the radiative response reflects the impact of the modified wet removal processes. The increased aerosol burdens improve agreement in aerosol total-column number concentrations for most high-latitude AERONET sites, but tend to progressively overestimate AOD and underestimate AE, suggesting that the model is overestimating the size of aerosol particles at those locations.

The increased aerosol loads for MOD1 and MOD2 significantly improve AOD with respect to satellite observations over the summer hemisphere, but lead to a significant overestimation over the winter hemisphere, indicating a failure in capturing the seasonal variability of aerosols over marine mid- and high-latitudes. A possible explanation is that the IFS, despite linking SU production to the oxidation of available dimethyl sulfide (DMS), has no representation of sea-borne marine organic aerosols. These are likely linked to photosynthetic activity of phytoplanktons (Sellegri et al., 2024) and are found to significantly contribute to spatio-temporal variability of cloud N_d (McCoy et al., 2015). Therefore, considering sea spray as only SS containing might result in an overestimated burden of SS, with boundary layer aerosols lacking the correct seasonal cycle.

The MOD1 and MOD2 tests have demonstrated high sensitivity of simulated N_d to the representation of aerosol removal by precipitation from mixed-phase clouds. However, despite the increased complexity, MOD1 and MOD2 are not able to provide a complete representation of the known aspects of the WBF process. In fact, particles released by evaporating droplets also incorporate information on microphysical processes occurring until evaporation, e.g. collection, collision-coalescence or nucleation, resulting in internal mixtures with increased particle size (Hoose et al., 2008). Such evolution cannot be effectively represented with the single-moment cloud scheme of the IFS, since no memory of cloud particle number concentrations is preserved. However, our investigation indicates that this is a candidate non-tuned process limiting the effectiveness of the N_d optimisation at high latitudes.

The optimal N_d values from ClBase3 optimisation perform markedly better than InCloud at mid- and high southern latitudes. This likely does not reflect better physical realism, because of the inconsistency with vertical tracer transport to cloud top (see

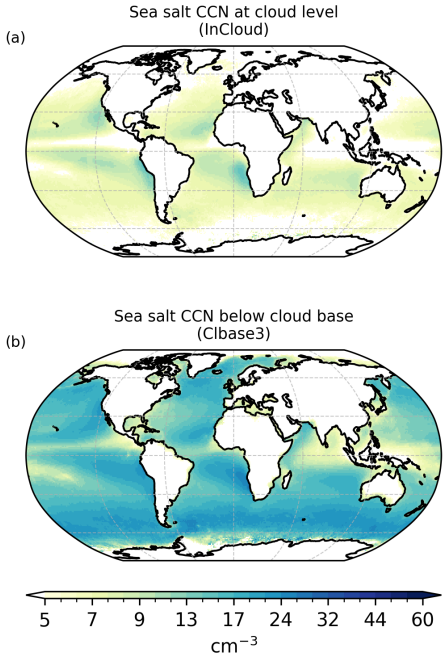

Figure 14. Mean N_d from sea salt fine (Ssf) CCN diagnosed during the offline optimisation procedure (2003–2020). The panels show aerosol diagnostics at cloud level (InCloud, a) and three model levels below cloud base (ClBase3, b), highlighting the different meridional distribution of diagnosed Ssf in the two setups.

990 discussion in Section 5), but rather a more meridionally-uniform aerosol background found below cloud base, than inside the cloud. To illustrate this point, Figure 14 shows the amount of diagnosed Ssf particles (represented with the prior PSDs) during the InCloud and ClBase3 setup. In principle, low Ssf number concentrations are expected, as sea-spray is secondary CCN provider (e.g. McFarquhar et al., 2021). However, coarse sea salt significantly impacts N_d in pristine regions via activation competition mechanisms of heterogeneous aerosol populations (Fossum et al., 2020), making a realistic representation of
995 marine aerosol profiles essential to predict N_d. While particle concentrations typically between $\approx 7\,\mathrm{cm}^{-3}$ and $\approx 20\,\mathrm{cm}^{-3}$ are found at cloud level in subtropical latitudes, the concentrations sharply fall below $5\,\mathrm{cm}^{-3}$ with increasing latitude. Such meridional contrast is not found when diagnosing Ssf CCN just below the cloud base (with significantly higher values up to $\approx 30\,\mathrm{cm}^{-3}$), so that for ClBase3 their concentrations over the SO are of similar or higher magnitude than subtropical values. As a result of this substantially different aerosol background, the optimisation for ClBase3 yields significantly better
1000 agreement although it does not guarantee physical consistency, highlighting the need for independent observational constraints. Nonetheless, this makes the ClBase3 approach a viable workaround for improved model N_d in IFS-COMPO until aerosol

concentrations inside clouds are improved, with the important caveat of a trade-off between correcting N_d biases and preserving consistency with optics and vertical transport of tracers.

8 Summary, outlook and conclusions

In this studywe showed that , we introduced an explicit representation of aerosol-cloud interactions (ACI)in a weather model can provide novel constraints on modelled aerosol processes. To do this, we introduced a lightweight aerosol activation scheme into the , limited to aerosol activation and the first indirect effect, in the ECMWF Integrated Forecasting System (IFS)used to implement , enabling cloud droplet number concentrations (N_d) to be used as an additional aerosol diagnostic. By combining a physically informed aerosol activation scheme with 18 years of satellite N_d retrievals from MODIS, we showed that N_d can constrains aerosol number concentrations for the Copernicus Atmosphere Monitoring Service (CAMS). Then, we optimized droplet number concentrations (Using this framework, we illustrated that a bulk aerosol scheme can reproduce realistic N_d) from CAMS , within limits imposed by the modelled aerosol particle size distributions (PSDs), vertical transport and wet removal.

We optimised the PSDs of CCN-providing aerosols using an 18-year-long series of offline diagnostic method, adjusting a small set of five free parameters using MODIS N_d retrievals. We finally combined the results of the optimization procedure with extensive observations of aerosols and observations. This method accounts for the co-location of aerosol and cloud profiles by combining stored output of prognostic aerosol simulations with reanalysis data, and consistently filters the same cloud regimes as in the N_d observations. The resulting PSDs substantially improve simulated N_d, while having only a limited impact on aerosol optical properties. The optimised PSDs were further evaluated against independent observations of optical properties from AERONET and satellites.

The optimisation procedure was unable to correct low N_d at high latitudes over the ocean, especially over the Southern Ocean, leading to a degradation in simulated top-of-atmosphere (TOA) all-sky radiative fluxes to evaluate otherwise poorly-observed aerosol processes. As a result, we identified possible issues associated with wildfire emissions, and we effectively evaluated an upgrade of the wet-scavenging parametrization of the model. The optimization procedure based on satellite observations corrects the prior model CCN number concentrations over the tropics by decreasing the PSD median radius for sulfates, while increasing it for organic matter and nitrates. Despite the substantial effect in number concentrations (up to a factor five) , the implied change in visible AOD is negligible. Using optimal PSDs highlights a few regions that appear more recalcitrant to the optimization procedure. The procedure failed also to correct the too low high-latitude CCN number concentrations . Results improved when the aerosols mixing ratios were diagnosed below cloud base, due to the steeply-declining profile of sea salt aerosols at the base of shortwave (SW) fluxes in online simulations. By performing online sensitivity tests, we showed that the simulated Southern Ocean N_d are highly sensitive to the representation of aerosol wet scavenging in mixed-phase clouds. We could track down a macroscopic clouds. Reduced scavenging efficiency in these regimes increases CCN concentrations within the clouds, offsetting most of the TOA SW degradation.

Despite a substantial reduction of the strong high-N_d overestimation (by a factor four to five) over north tropical and central Africato the carbonaceous aerosol emissions during the wildfire seasonbias over tropical Africa, the optimised N_d still show residual positive biases, although within the estimated observational uncertainty. Both observed and modelled N_d during periods of maximum residual bias are strongly correlated with carbonaceous emissions from assimilated wildfires in the model.

Moreover, data from AERONET stations suggest that the model is not generally overpredicting AOD, but rather overestimating the typical particle size of the finer ($< 0.5\ \mu m$) carbonaceous aerosol . We suggest that this hints at potential improvements of the description of pristine and aged aerosols from wildfires, including the possibility to represent smaller pristine soot particles and larger, eventually the optimal PSD returned for organic matter (OM) aerosol is inconsistent with independent AERONET observations over tropical Africa. This likely reflects limitations in the model representaton of black carbon ageing processes, that do not capture the clustering over time of soot particles into larger, internally-mixed aged aerosol. Possible future investigations could concern the accuracy of the described wildfire regime, as well as smoke plume properties, with downstream impact on carbonaceous aerosol vertical profiles and ageing timescales. To illustrate the diagnostic potential of ACI for constraining CAMS aerosol processes, we experimented two model versions that introduced modifications of the wet scavenging scheme. These target process representations that led to overestimated scavenged aerosol mass fraction in mixed-phase clouds. These changes improved the number mixing ratio of CCN inside mixed-phase clouds, as well as the simulated total-column aerosol particle numbers and AOD during the austral summer. This resulted in successful elimination of the top-of-the-atmosphere broadband shortwave bias over the Southern Ocean introduced by using the activation scheme with the CAMS aerosols in the current model version. CAMS aerosols can overall produce realistic CCN number concentrations and, in turn, aerosol. Excluding black carbon from the optimisation yields comparable N_d, without degrading aerosol optical properties.

These results indicate that achieving physically consistent and realistic N_d values, if number-to-mass conversion factors are calculated from optimized PSDs. The optimization procedure also offers valuable information on number concentrations of CAMS aerosols, that would otherwise be weakly constrained by traditional AOD observations. The optimized PSDs showed that the CAMS aerosols description over tropical and mid-latitudes seas could significantly benefit from the introduction of an accumulation mode to represent aging of sulfate, nitrate and organic matter aerosolspecies. In order to produce realistic N_d values over the Southern Ocean, the CAMS aerosol need to improve air composition at cloud level, that we show might be done with a more sophisticated parametrization of wet scavenging in at mid- and high-latitudes over pristine marine environments requires improved aerosol availability at cloud level. Excessive wet removal of aerosols in mixed-phase clouds. Such modifications also increase AOD over sea at high latitudesclouds emerges as a key regulator of aerosol indirect effects in the region, indicating a possible area for development in the CAMS aerosol system. Future improvements should also address deficiencies in the representation of marine aerosol sources, speciation and seasonality, including the potential role of biogenic primary marine organic aerosol. In the tropics, the results highlight the need to further constrain carbonaceous aerosol emissions and ageing, to better represent the impact of wildfire emissions on cloud microphysics. Future work will also be needed to address updraft variability relevant for aerosol activation in updraft-limited regimes, which is beneficial in the summer hemisphere, but detrimental in the winter hemisphere. This suggests that the simulated seasonal cycle of aerosol emissions might need improvement. The CAMS aerosols tend to underpredict AE over high latitude seas, which is probably due to too large AOD contribution from coarse sea salt ($r \geq 1\ \mu m$). Such evidence might point at issues with the aerosol speciation in these regions. Possible areas of improvement could involve the seasonal cycle of emissions for dimethyl sulfide (DMS) and the amount of biogenic marine organic aerosol contained in sea spray.

Code availability. The IFS code is the intellectual property of ECMWF and its member states, and therefore it is not publicly available. Access to the IFS code updated to version CY48R1 can be obtained from ECMWF under a free OpenIFS licence. The code used to simulate optical properties uses the Scott Prahl's Miepython library ().

currently poorly constrained by observations.

As a final perspective, improving aerosol-cloud interaction representations in bulk aerosol schemes will require coordinated advances across multiple aspects of aerosol representation and associated processes. At the same time, satellite N_d observations emerge from this study as a valuable diagnostic tool that, combined with multi-spectral aerosol observations from ground-based photometers and satellite imagers, can help constrain aerosol number concentrations and associated processes that are only weakly informed by standard AOD validations.

Code and data availability. The IFS code is the intellectual property of ECMWF and its member states, and therefore version CY49R1 used for this study is not yet publicly available. However, access to the IFS code, including IFS-COMPO, updated to version CY48R1 is provided by the OpenIFS project (https://github.com/ecmwf-ifs/openifs). The code used to simulate optical properties uses Scott Prahl's Miepython library (https://github.com/scottprahl/miepython). The lookup table for activation used for this study can be accessed at https://doi.org/10.5281/zenodo.20051869. The code used for the offline optimisation is available at https://github.com/pandreozzz/optimind.

Appendix A: Conversion from mixed bulk-bin representation to split bulk representation of sea salt aerosol

CAMS Sea salt aerosol is represented by a bimodal distribution whose domain is partitioned into three intervals, or bins. Each of these bins is assigned to a different tracer ; so that three sea salt aerosol species are defined: size intervals (bins), associated with a separate tracer (fine, mediumand coarse (, coarse - bins 1 to 3). This means that we need to define a function mapping For use in the activation scheme, a mapping from the mixed bulk-bin to the bulk representation used for the activation scheme. a bulk monomodal representation is required.

In general, it is not possible to find a conversion strategy that preserves such conversion does not preserve all moments of the distribution, due to the fact that the since the mixed bulk-bin representation allows discontinuities at the boundaries of each interval bin bin boundaries. In this study, we decided to map the three bins of a bimodal distribution onto the two modes of the same distribution, thus original bimodal distribution, thereby defining two sea salt ccn speciesto use in the activation scheme. Let $n_i(r) = \mathrm{d}N/\mathrm{d}r(r)$ the $b$species.

Let $n_i(r) = \mathrm{d}N_i/\mathrm{d}r(r)$ the i-th mode of the original number PSD, α_i the relative weight assigned to the mode ($\sum_i \alpha_i = 1$) and Φ_b the interval defining the domain for the bin species size interval of the bin b. The total mass of a species M_b bin b is given bythe sum of the masses projecting on the two PSD modes: :

$$M_b = \sum_i M_{b,i} = \sum_i \frac{4}{3}\pi\rho \int_{\Phi_b} r^3 \alpha_i n_i(r)\,\mathrm{d}r \tag{A1}$$

where ρ is the mass density. By taking the ratio $q_{b,i} = M_{b,i}/M_b$ one knows which fraction of the mass of the bin species b must be assigned to the split i-th mode of the original distribution. This results in the fractional contributions of the three sea salt bins to the two sea salt ccn species. However, while this method ensures that the mapping across representations bimodal distribution.

While this approach conserves total mass by construction, it does not constrain particle numbers. The only (particular) case when particle numbers are preserved is when the ratio between the mass concentrationsof the three sea salt species is such that the merged distribution resulting from it is smooth. number concentrations, except for the special case where the relative bin mass contributions lead to a smooth merged distribution.

Appendix B: Relationship between AOD and particle numbers number concentration in a bulk representation

Optical The optical thickness per unit mass(here indicated with , here denoted by t) of a unit volume homogeneously filled by a total mass M of , for an aerosol species given by: with total mass M_a, is given by

$$t \equiv \tau/M_a = \pi \frac{N_a}{M_a} \int r^2 Q_{\text{ext}} n(r)\, \mathrm{d}r \tag{B1}$$

where N_a is the total number of aerosol particles, $n(r)$ is the normalized number distribution . If we consider as a rough approximation (for an ideal case with small enough σ) $Q \approx q\, r^k$ (where $k = 6$ in and Q_{ext} the Mie extinction efficiency. In the limit of narrow distributions, and for purely real refractive index, we can replace Q_{ext} with a local approximation dominated by a term $\approx q\, r^k$, with q and k real numbers. In the Rayleigh scattering regime , for purely real refractive index) and use the notable $k \approx 6$; at the Mie resonance peak $q \approx 4$ and $k \approx 0$; in the geometric optics regime $q \approx 2$ and $k \approx 0$. Using standard expressions for the momenta of a moments of the log-normal distribution : $n(r)$ yields

$$\begin{aligned} t &\approx \frac{q}{4/3\pi\rho} \frac{E[r^{k+2}]}{E[r^3]} \\ &\approx \frac{q}{4/3\pi\rho} r_{\text{med}}^{k-1}\, e^{(k^2+2k-5)\ln^2\sigma} \end{aligned} \tag{B2}$$

More straightforwardly, the where r_{med} and σ are the median and geometric standard deviations of $n(r)$.

The number of particles per unit mass(hereby with , denoted by n_a) is given , is obtained from the identity between total mass M M_a and number of particles N: N_a:

$$n_a \equiv \frac{N_a}{M_a} = \frac{1}{4/3\pi\rho} r_{\text{med}}^{-3}\, e^{-9\ln^2\sigma} \tag{B3}$$

The amount of droplet number of cloud droplets is then a non-trivial but monotonic function of n_a. These relationships illustrate that, in , and is calculated by an activation scheme.

In a bulk representation, increasing/decreasing scaling the burden of an aerosol species determines a proportional variation in both proportionally affects τ and N_a. However, changing μ changes in r_{med} and σ impacts τ and N_a in regime-depending

directions: affect t and n_a differently depending on the optical regime:

$$\frac{\partial t}{\partial \ln r_{\text{med}}} \approx (k-1)\, t \tag{B4}$$

$$\frac{\partial t}{\partial \ln \sigma} \approx 2(k^2+2k-5) \ln\sigma\, t \tag{B5}$$

$$\frac{\partial n_a}{\partial \ln r_{\text{med}}} = -3\, n_a \tag{B6}$$

$$\frac{\partial n_a}{\partial \ln \sigma} = -18 \ln\sigma\, n_a \tag{B7}$$

In the case of limit $r \ll \lambda$, it is asymptotically satisfied that Q_{sca} Q_{ext} grows faster than linear, linearly (i.e. $k > 1$, with $k = 6$ for the Rayleigh non-absorbing regime. In all these cases increasing /decreasing). In this case, increasing the median radius $r_{\text{med}} = \log(\mu)$ inversely affects r_{med} decreases the optical thickness of the speciesper unit mass t. For larger radii, In the geometric optics regime, $q \approx 2$, $k \approx 0$, so that a smaller median radius implies the tracer to be optically thicker. The ratio between light wavelength and particle size, as well as the orientation of the refractive index in complex space, define the response regime for AOD to PSD definition. leads to a larger optical thickness. Therefore, both the wavelength-to-size ratio and the refractive index determine how AOD responds to the particle size distribution.

Appendix C: Aerosol mass burden errors from activation rates in the IFS wet scavenging scheme.

The

The IFS wet scavenging scheme is expected to underestimate removal of all species we used as CCN except BC. In fact, for each aerosol the assigns a prescribed dissolved mass fraction for warm-phase conditions is given by a prescribed value: namely to each aerosol species: 0.9 for SSsea salt (SS), 0.8 AM and NIfor ammonium (AM) and nitrate (NI), 0.7 for every all other hydrophilic species. Typical dissolved activated mass fraction values provided by the activation scheme are However, the parcel model yields activated mass fractions close to 1 for all species excluding black carbon , in line most species except black carbon (BC), consistent with approaches adopted in global chemical transport models (see e.g. Wang et al. (2014b)). This is due to the mass-domination of the large fraction of The reason for this is that most aerosol species , even those with relatively-low hygroscopicity like OM, while significant are dominated in mass by their large particle fraction, even for relatively low hygroscopicity species like organic matter (OM). In contrast, BC is characterised by substantial variability in activated mass fraction is associated with BC, due to due to its low hygroscopicity and, most importantly, small typical its typically small particle size. (see figure **??**) . Therefore, As a result, the IFS wet scavenging scheme is expected to underestimate aerosol removal of all species except BC. To quantify this effect, we performed an IFS-COMPO online experiment (with meteorology reinitialised every day from ERA5 and aerosols from previous day) for the period November-December 2023. In this experiment, the wet scavenging scheme diagnoses the dissolved mass fraction from the activation scheme rather than using the prescribed values. Figure C1 shows the global relative change in total column aerosol mass given by a simulation where the mass scavenging rates were diagnosed by the wet-scavenging scheme from the aerosol activation scheme; the actual impact is limited within 10%for most species and within 80% for NI and OM. This means that the too low mass scavenging rates

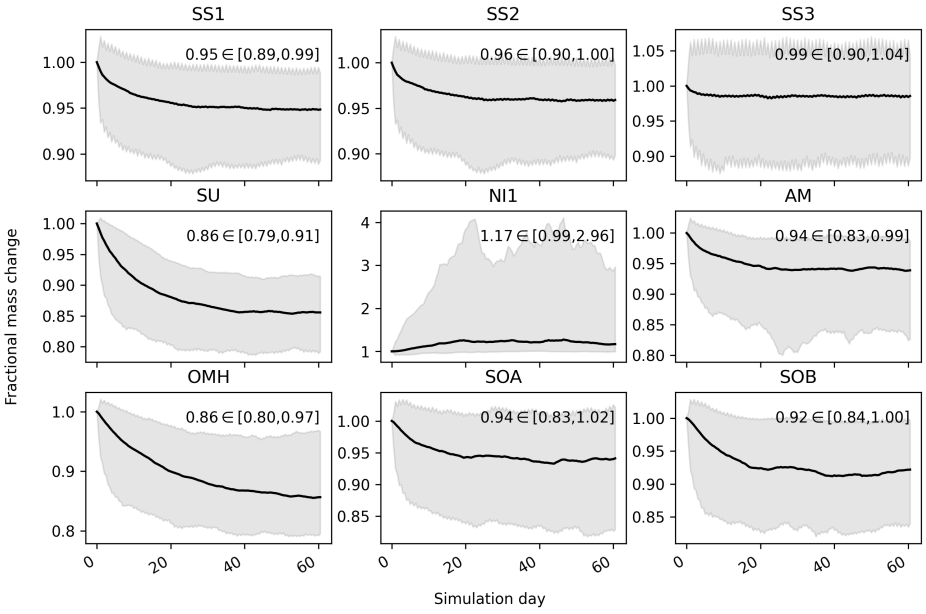

Figure C1. Relative change in total-column aerosol mass of several species from using in-cloud scavenging rates diagnosed by the aerosol activation scheme instead of the default fixed IFS values. Solid line is the median relative change (experiment divided by control), shadings are the global 5th and 95th percentiles of the relative change. For each panel, values for the last time-step (day 60) are reported.

of the current . The magnitude of the reduction remains typically within 15%, overall confirming that the IFS wet scavenging scheme can explain only a small fraction of the excess particle numbers for sulfates, nitrates and organics CCN. underestimates removal rates, but with a limited global impact.

Author contributions. PA: conceptualization, data curation, formal analysis, investigation, methodology, software, visualization, writing (original draft preparation); MDF: conceptualization, methodology, software, writing (review and editing); RJH: conceptualization, supervision, writing (review and editing); RMF: conceptualization, supervision, writing (review and editing); AAH: writing (review and editing); SR: data curation, writing (review and editing); BB: supervision, writing (review and editing); UL: supervision, writing (review and editing)

Competing interests. The authors declare that they have no conflict of interest.

Acknowledgements. We thank the AERONET PIs Alexander Mangold, Alexis Merlaud, Anatoli Chaikovsky, Corinne Galy-Lacaux, David Lehmann, Elena Lind, Fabiola Tata, Grzegorz Karasinski, Ihab Abboud, Jacobo Salvador, Lynn Ma, Margarida Fernandes Ventura, Michel Van Roozendal, Norm O'Neill, Patric Seifert, Pawan Gupta, Philippe Goloub, Piotr Glowacki, Piotr Sobolewski, Pr Veronique Yoboue,

Rachel T. Pinker, Raul D'Elia, Raul R. Cordero, Richard Damoah, Rick Wagener, Victoria E. Cachorro Revilla, Vitali Fioletov and their staff for establishing and maintaining the sites used for this investigation. We thank the community of developers of the Matplotlib and Xarray projects. We

We acknowledge the work of Crameri et al. (2020) for the colourmaps we used for plotting data.

We thank the CAMS researchers at ECMWF, with special regards to in particular Enza di Tomasoand Mark Parringtonfor the discussions about the current state of GFAS , Mark Parrington, Emmanuele Russo and Johannes Flemmingfor the frequent feedbacks on the development of this research.

Financial support.

This study was conducted within the STEP-UP! Fellowship programme funded by the Deutscher Wetterdienst (DWD) and Forschungszentrum Jülich (FZJ) and materially supported by ECMWF in collaboration with the Center for Earth System Observation and Computational analysis (CESOC).

References

Ahlgrimm, M., Forbes, R. M., Hogan, R. J., and Sandu, I.: Understanding Global Model Systematic Shortwave Radiation Errors in Subtropical Marine Boundary Layer Cloud Regimes, Journal of Advances in Modeling Earth Systems, 10, 2042–2060, https://doi.org/10.1029/2018MS001346, 2018.

Ahola, J., Raatikainen, T., Alper, M. E., Keskinen, J.-P., Kokkola, H., Kukkurainen, A., Lipponen, A., Liu, J., Nordling, K., Partanen, A.-I., Romakkaniemi, S., Räisänen, P., Tonttila, J., and Korhonen, H.: Technical Note: Parameterising Cloud Base Updraft Velocity of Marine Stratocumuli, Atmospheric Chemistry and Physics, 22, 4523–4537, https://doi.org/10.5194/acp-22-4523-2022, 2022.

Albrecht, B. A.: Aerosols, Cloud Microphysics, and Fractional Cloudiness, Science, 245, 1227–1230, https://doi.org/10.1126/science.245.4923.1227, 1989.

Baklanov, A., Brunner, D., Carmichael, G., Flemming, J., Freitas, S., Gauss, M., Hov, O. y., Mathur, R., Schlünzen, K. H., Seigneur, C., and Vogel, B.: Key Issues for Seamless Integrated Chemistry–Meteorology Modeling, Bulletin of the American Meteorological Society, 98, 2285–2292, https://doi.org/10.1175/BAMS-D-15-00166.1, 2017.

Barahona, D., Molod, A., Bacmeister, J., Nenes, A., Gettelman, A., Morrison, H., Phillips, V., and Eichmann, A.: Development of Two-Moment Cloud Microphysics for Liquid and Ice within the NASA Goddard Earth Observing System Model (GEOS-5), Geoscientific Model Development, 7, 1733–1766, https://doi.org/10.5194/gmd-7-1733-2014, 2014.

Bellouin, N., Rae, J., Jones, A., Johnson, C., Haywood, J., and Boucher, O.: Aerosol Forcing in the Climate Model Intercomparison Project (CMIP5) Simulations by HadGEM2-ES and the Role of Ammonium Nitrate, Journal of Geophysical Research, 116, D20 206, https://doi.org/10.1029/2011JD016074, 2011.

Bellouin, N., Quaas, J., Gryspeerdt, E., Kinne, S., Stier, P., Watson-Parris, D., Boucher, O., Carslaw, K. S., Christensen, M., Daniau, A.-L., Dufresne, J.-L., Feingold, G., Fiedler, S., Forster, P., Gettelman, A., Haywood, J. M., Lohmann, U., Malavelle, F., Mauritsen, T., McCoy, D. T., Myhre, G., Mülmenstädt, J., Neubauer, D., Possner, A., Rugenstein, M., Sato, Y., Schulz, M., Schwartz, S. E., Sourdeval, O., Storelvmo, T., Toll, V., Winker, D., and Stevens, B.: Bounding Global Aerosol Radiative Forcing of Climate Change, Reviews of Geophysics, 58, e2019RG000 660, https://doi.org/10.1029/2019RG000660, 2020.

Benedetti, A., Morcrette, J., Boucher, O., Dethof, A., Engelen, R. J., Fisher, M., Flentje, H., Huneeus, N., Jones, L., Kaiser, J. W., Kinne, S., Mangold, A., Razinger, M., Simmons, A. J., and Suttie, M.: Aerosol analysis and forecast in the European Centre for Medium-Range Weather Forecasts Integrated Forecast System: 2. Data assimilation, Journal of Geophysical Research: Atmospheres, 114, 2008JD011 115, https://doi.org/10.1029/2008JD011115, 2009.

Bennartz, R. and Rausch, J.: Global and Regional Estimates of Warm Cloud Droplet Number Concentration Based on 13 Years of AQUA-MODIS Observations, Atmospheric Chemistry and Physics, 17, 9815–9836, https://doi.org/10.5194/acp-17-9815-2017, 2017.

Blake, L., Arola, A., Benedictow, A., Bennouna, Y., Bouarar, I., Cuevas, E., Errera, Q., Eskes, H., Griesfeller, J., Ilic, L., Kapsomenakis, J., Langerock, B., Mortier, A., Pison, I., Pitkänen, M., Richter, A., Schoenhardt, A., Schulz, M., Thouret, V., Tsikerdekis, A., Warneke, T., and Zerefos, C.: Validation Report of the CAMS Global Reanalysis of Aerosols and Reactive Trace Gases, Years 2003-2024, https://doi.org/10.24380/VV0T-8TCG, 2025.

Block, K., Haghighatnasab, M., Partridge, D. G., Stier, P., and Quaas, J.: Cloud Condensation Nuclei Concentrations Derived from the CAMS Reanalysis, Earth System Science Data, 16, 443–470, https://doi.org/10.5194/essd-16-443-2024, 2024.

Bodas-Salcedo, A., Williams, K. D., Ringer, M. A., Beau, I., Cole, J. N. S., Dufresne, J.-L., Koshiro, T., Stevens, B., Wang, Z., and Yokohata, T.: Origins of the Solar Radiation Biases over the Southern Ocean in CFMIP2 Models*, Journal of Climate, 27, 41–56, https://doi.org/10.1175/JCLI-D-13-00169.1, 2014.

Bozzo, A., Benedetti, A., Flemming, J., Kipling, Z., and Rémy, S.: An aerosol climatology for global models based on the tropospheric aerosol scheme in the Integrated Forecasting System of ECMWF, Geoscientific Model Development, 13, 1007–1034, https://doi.org/10.5194/gmd-13-1007-2020, 2020.

C3S: ERA5 Hourly Data on Single Levels from 1940 to Present, https://doi.org/10.24381/CDS.ADBB2D47, 2018.

Crameri, F., Shephard, G. E., and Heron, P. J.: The Misuse of Colour in Science Communication, Nature Communications, 11, 5444, https://doi.org/10.1038/s41467-020-19160-7, 2020.

Deardorff, J. W.: Convective Velocity and Temperature Scales for the Unstable Planetary Boundary Layer and for Rayleigh Convection, Journal of the Atmospheric Sciences, 27, 1211–1213, https://doi.org/10.1175/1520-0469(1970)027<1211:CVATSF>2.0.CO;2, 1970.

Doelling, D.: CERES Energy Balanced and Filled (EBAF) TOA Monthly Means Data in netCDF Edition4.2, https://doi.org/10.5067/TERRA-AQUA-NOAA20/CERES/EBAF-TOA_L3B004.2, 2022.

Dubovik, O. and King, M. D.: A flexible inversion algorithm for retrieval of aerosol optical properties from Sun and sky radiance measurements, Journal of Geophysical Research: Atmospheres, 105, 20 673–20 696, https://doi.org/10.1029/2000JD900282, 2000.

ECMWF: IFS Documentation CY49R1 - Part VIII: Atmospheric Composition, Tech. rep., https://doi.org/10.21957/D13AF18259, publisher: ECMWF, 2024a.

ECMWF: IFS Documentation CY49R1 - Part IV: Physical Processes, Tech. rep., https://doi.org/10.21957/C731EE1102, publisher: ECMWF, 2024b.

Field, P. R., Hill, A., Shipway, B., Furtado, K., Wilkinson, J., Miltenberger, A., Gordon, H., Grosvenor, D. P., Stevens, R., and Van Weverberg, K.: Implementation of a double moment cloud microphysics scheme in the UK met office regional numerical weather prediction model, Quarterly Journal of the Royal Meteorological Society, 149, 703–739, https://doi.org/10.1002/qj.4414, 2023.

Flemming, J., Huijnen, V., Arteta, J., Bechtold, P., Beljaars, A., Blechschmidt, A.-M., Diamantakis, M., Engelen, R. J., Gaudel, A., Inness, A., Jones, L., Josse, B., Katragkou, E., Marecal, V., Peuch, V.-H., Richter, A., Schultz, M. G., Stein, O., and Tsikerdekis, A.: Tropospheric Chemistry in the Integrated Forecasting System of ECMWF, Geoscientific Model Development, 8, 975–1003, https://doi.org/10.5194/gmd-8-975-2015, 2015.

Forkel, M., Wessollek, C., Huijnen, V., Andela, N., De Laat, A., Kinalczyk, D., Marrs, C., Van Wees, D., Bastos, A., Ciais, P., Fawcett, D., Kaiser, J. W., Klauberg, C., Kutchartt, E., Leite, R., Li, W., Silva, C., Sitch, S., Goncalves De Souza, J., Zaehle, S., and Plummer, S.: Burning of Woody Debris Dominates Fire Emissions in the Amazon and Cerrado, Nature Geoscience, 18, 140–147, https://doi.org/10.1038/s41561-024-01637-5, 2025.

Fossum, K. N., Ovadnevaite, J., Ceburnis, D., Preißler, J., Snider, J. R., Huang, R.-J., Zuend, A., and O'Dowd, C.: Sea-spray regulates sulfate cloud droplet activation over oceans, npj Climate and Atmospheric Science, 3, 14, https://doi.org/10.1038/s41612-020-0116-2, 2020.

Ghan, S. J., Abdul-Razzak, H., Nenes, A., Ming, Y., Liu, X., Ovchinnikov, M., Shipway, B., Meskhidze, N., Xu, J., and Shi, X.: Droplet Nucleation: Physically-based Parameterizations and Comparative Evaluation: DROPLET NUCLEATION, Journal of Advances in Modeling Earth Systems, 3, https://doi.org/10.1029/2011MS000074, 2011.

Golaz, J.-C., Salzmann, M., Donner, L. J., Horowitz, L. W., Ming, Y., and Zhao, M.: Sensitivity of the Aerosol Indirect Effect to Subgrid Variability in the Cloud Parameterization of the GFDL Atmosphere General Circulation Model AM3, Journal of Climate, 24, 3145–3160, https://doi.org/10.1175/2010JCLI3945.1, 2011.

Gordon, H., Glassmeier, F., and T. McCoy, D.: An Overview of Aerosol-Cloud Interactions, in: Geophysical Monograph Series, edited by Sullivan, S. C. and Hoose, C., pp. 13–45, Wiley, 1 edn., ISBN 978-1-119-70031-9 978-1-119-70035-7, https://doi.org/10.1002/9781119700357.ch2, 2023.

Grosvenor, D. P. and Wood, R.: The effect of solar zenith angle on MODIS cloud optical and microphysical retrievals within marine liquid water clouds, Atmospheric Chemistry and Physics, 14, 7291–7321, https://doi.org/10.5194/acp-14-7291-2014, 2014.

Grosvenor, D. P., Sourdeval, O., and Wood, R.: Parameterizing cloud top effective radii from satellite retrieved values, accounting for vertical photon transport: quantification and correction of the resulting bias in droplet concentration and liquid water path retrievals, Atmospheric Measurement Techniques, 11, 4273–4289, https://doi.org/10.5194/amt-11-4273-2018, 2018a.

Grosvenor, D. P., Sourdeval, O., Zuidema, P., Ackerman, A., Alexandrov, M. D., Bennartz, R., Boers, R., Cairns, B., Chiu, J. C., Christensen, M., Deneke, H., Diamond, M., Feingold, G., Fridlind, A., Hünerbein, A., Knist, C., Kollias, P., Marshak, A., McCoy, D., Merk, D., Painemal, D., Rausch, J., Rosenfeld, D., Russchenberg, H., Seifert, P., Sinclair, K., Stier, P., van Diedenhoven, B., Wendisch, M., Werner, F., Wood, R., Zhang, Z., and Quaas, J.: Remote Sensing of Droplet Number Concentration in Warm Clouds: A Review of the Current State of Knowledge and Perspectives, Reviews of Geophysics, 56, 409–453, https://doi.org/10.1029/2017RG000593, 2018b.

Gryspeerdt, E., McCoy, D., Crosbie, E., Moore, R. H., Nott, G. J., Painemal, D., Small-Griswold, J., Sorooshian, A., and Ziemba, L.: Cloud Droplet Number Concentration, Calculated from the MODIS (Moderate Resolution Imaging Spectroradiometer) Cloud Optical Properties Retrieval and Gridded Using Different Sampling Strategies, https://doi.org/10.5285/864A46CC65054008857EE5BB772A2A2B, 2022a.

Gryspeerdt, E., McCoy, D. T., Crosbie, E., Moore, R. H., Nott, G. J., Painemal, D., Small-Griswold, J., Sorooshian, A., and Ziemba, L.: The impact of sampling strategy on the cloud droplet number concentration estimated from satellite data, Atmospheric Measurement Techniques, 15, 3875–3892, https://doi.org/10.5194/amt-15-3875-2022, 2022b.

Gupta, P., Remer, L. A., Levy, R. C., and Mattoo, S.: Validation of MODIS 3 km land aerosol optical depth from NASA's EOS Terra and Aqua missions, Atmospheric Measurement Techniques, 11, 3145–3159, https://doi.org/10.5194/amt-11-3145-2018, 2018.

Hersbach, H., Bell, B., Berrisford, P., Hirahara, S., Horányi, A., Muñoz Sabater, J., Nicolas, J., Peubey, C., Radu, R., Schepers, D., Simmons, A., Soci, C., Abdalla, S., Abellan, X., Balsamo, G., Bechtold, P., Biavati, G., Bidlot, J., Bonavita, M., De Chiara, G., Dahlgren, P., Dee, D., Diamantakis, M., Dragani, R., Flemming, J., Forbes, R., Fuentes, M., Geer, A., Haimberger, L., Healy, S., Hogan, R. J., Hólm, E., Janisková, M., Keeley, S., Laloyaux, P., Lopez, P., Lupu, C., Radnoti, G., De Rosnay, P., Rozum, I., Vamborg, F., Villaume, S., and Thépaut, J.-N.: The ERA5 Global Reanalysis, Quarterly Journal of the Royal Meteorological Society, 146, 1999–2049, https://doi.org/10.1002/qj.3803, 2020.

Hogan, R. J., Grant, A. L. M., Illingworth, A. J., Pearson, G. N., and O'Connor, E. J.: Vertical Velocity Variance and Skewness in Clear and Cloud-topped Boundary Layers as Revealed by Doppler Lidar, Quarterly Journal of the Royal Meteorological Society, 135, 635–643, https://doi.org/10.1002/qj.413, 2009.

Holben, B., Eck, T., Slutsker, I., Tanré, D., Buis, J., Setzer, A., Vermote, E., Reagan, J., Kaufman, Y., Nakajima, T., Lavenu, F., Jankowiak, I., and Smirnov, A.: AERONET—A Federated Instrument Network and Data Archive for Aerosol Characterization, Remote Sensing of Environment, 66, 1–16, https://doi.org/10.1016/S0034-4257(98)00031-5, 1998.

Hoose, C., Lohmann, U., Stier, P., Verheggen, B., and Weingartner, E.: Aerosol processing in mixed-phase clouds in ECHAM5-HAM: Model description and comparison to observations, Journal of Geophysical Research: Atmospheres, 113, 2007JD009 251, https://doi.org/10.1029/2007JD009251, 2008.

Hoppel, W. A., Fitzgerald, J. W., Frick, G. M., Larson, R. E., and Mack, E. J.: Aerosol Size Distributions and Optical Properties Found in the Marine Boundary Layer over the Atlantic Ocean, Journal of Geophysical Research: Atmospheres, 95, 3659–3686, https://doi.org/10.1029/JD095iD04p03659, 1990.

Hsu, N. C., Jeong, M.-J., Bettenhausen, C., Sayer, A. M., Hansell, R., Seftor, C. S., Huang, J., and Tsay, S.-C.: Enhanced Deep Blue Aerosol Retrieval Algorithm: The Second Generation, Journal of Geophysical Research: Atmospheres, 118, 9296–9315, https://doi.org/10.1002/jgrd.50712, 2013.

Jones, A., Roberts, D. L., Woodage, M. J., and Johnson, C. E.: Indirect Sulphate Aerosol Forcing in a Climate Model with an Interactive Sulphur Cycle, Journal of Geophysical Research: Atmospheres, 106, 20 293–20 310, https://doi.org/10.1029/2000JD000089, 2001.

Kaiser, J. W., Heil, A., Andreae, M. O., Benedetti, A., Chubarova, N., Jones, L., Morcrette, J.-J., Razinger, M., Schultz, M. G., Suttie, M., and Van Der Werf, G. R.: Biomass Burning Emissions Estimated with a Global Fire Assimilation System Based on Observed Fire Radiative Power, Biogeosciences, 9, 527–554, https://doi.org/10.5194/bg-9-527-2012, 2012.

Khairoutdinov, M. and Kogan, Y.: A New Cloud Physics Parameterization in a Large-Eddy Simulation Model of Marine Stratocumulus, Monthly Weather Review, 128, 229–243, https://doi.org/10.1175/1520-0493(2000)128<0229:ANCPPI>2.0.CO;2, 2000.

Lagarias, J. C., Reeds, J. A., Wright, M. H., and Wright, P. E.: Convergence Properties of the Nelder–Mead Simplex Method in Low Dimensions, SIAM Journal on Optimization, 9, 112–147, https://doi.org/10.1137/S1052623496303470, 1998.

Leaitch, W. R., Strapp, J. W., Isaac, G. A., and Hudson, J. G.: Cloud Droplet Nucleation and Cloud Scavenging of Aerosol Sulphate in Polluted Atmospheres, Tellus B, 38B, 328–344, https://doi.org/10.1111/j.1600-0889.1986.tb00258.x, 1986.

Levy, R. C., Mattoo, S., Munchak, L. A., Remer, L. A., Sayer, A. M., Patadia, F., and Hsu, N. C.: The Collection 6 MODIS Aerosol Products over Land and Ocean, Atmospheric Measurement Techniques, 6, 2989–3034, https://doi.org/10.5194/amt-6-2989-2013, 2013.

Liu, M. and Matsui, H.: Improved Simulations of Global Black Carbon Distributions by Modifying Wet Scavenging Processes in Convective and Mixed-Phase Clouds, Journal of Geophysical Research: Atmospheres, 126, e2020JD033 890, https://doi.org/10.1029/2020JD033890, 2021.

Liu, Y., Daum, P. H., McGraw, R., and Wood, R.: Parameterization of the Autoconversion Process. Part II: Generalization of Sundqvist-Type Parameterizations, Journal of the Atmospheric Sciences, 63, 1103–1109, https://doi.org/10.1175/JAS3675.1, 2006.

Luo, G., Yu, F., and Schwab, J.: Revised treatment of wet scavenging processes dramatically improves GEOS-Chem 12.0.0 simulations of surface nitric acid, nitrate, and ammonium over the United States, Geoscientific Model Development, 12, 3439–3447, https://doi.org/10.5194/gmd-12-3439-2019, 2019.

Maddux, B. C., Ackerman, S. A., and Platnick, S.: Viewing Geometry Dependencies in MODIS Cloud Products, Journal of Atmospheric and Oceanic Technology, 27, 1519–1528, https://doi.org/10.1175/2010JTECHA1432.1, 2010.

Martin, G. M., Johnson, D. W., and Spice, A.: The Measurement and Parameterization of Effective Radius of Droplets in Warm Stratocumulus Clouds, Journal of the Atmospheric Sciences, 51, 1823–1842, https://doi.org/10.1175/1520-0469(1994)051<1823:TMAPOE>2.0.CO;2, 1994.

McCoy, D. T., Burrows, S. M., Wood, R., Grosvenor, D. P., Elliott, S. M., Ma, P.-L., Rasch, P. J., and Hartmann, D. L.: Natural aerosols explain seasonal and spatial patterns of Southern Ocean cloud albedo, Science Advances, 1, e1500 157, https://doi.org/10.1126/sciadv.1500157, 2015.

McCoy, D. T., Bender, F. A.-M., Grosvenor, D. P., Mohrmann, J. K., Hartmann, D. L., Wood, R., and Field, P. R.: Predicting Decadal Trends in Cloud Droplet Number Concentration Using Reanalysis and Satellite Data, Atmospheric Chemistry and Physics, 18, 2035–2047, https://doi.org/10.5194/acp-18-2035-2018, 2018.

McFarquhar, G. M., Bretherton, C. S., Marchand, R., Protat, A., DeMott, P. J., Alexander, S. P., Roberts, G. C., Twohy, C. H., Toohey, D., Siems, S., Huang, Y., Wood, R., Rauber, R. M., Lasher-Trapp, S., Jensen, J., Stith, J. L., Mace, J., Um, J., Järvinen, E., Schnaiter, M., Gettelman, A., Sanchez, K. J., McCluskey, C. S., Russell, L. M., McCoy, I. L., Atlas, R. L., Bardeen, C. G., Moore, K. A., Hill, T. C. J., Humphries, R. S., Keywood, M. D., Ristovski, Z., Cravigan, L., Schofield, R., Fairall, C., Mallet, M. D., Kreidenweis, S. M., Rainwater, B., D'Alessandro, J., Wang, Y., Wu, W., Saliba, G., Levin, E. J. T., Ding, S., Lang, F., Truong, S. C. H., Wolff, C., Haggerty, J., Harvey, M. J., Klekociuk, A. R., and McDonald, A.: Observations of Clouds, Aerosols, Precipitation, and Surface Radiation over the Southern Ocean: An Overview of CAPRICORN, MARCUS, MICRE, and SOCRATES, Bulletin of the American Meteorological Society, 102, E894–E928, https://doi.org/10.1175/BAMS-D-20-0132.1, 2021.

Menon, S., Genio, A. D. D., Koch, D., and Tselioudis, G.: GCM Simulations of the Aerosol Indirect Effect: Sensitivity to Cloud Parameterization and Aerosol Burden, Journal of the Atmospheric Sciences, 59, 692–713, https://doi.org/10.1175/1520-0469(2002)059<0692:GSOTAI>2.0.CO;2, 2002.

Mitchell, D. L.: Parameterization of the Mie Extinction and Absorption Coefficients for Water Clouds, Journal of the Atmospheric Sciences, 57, 1311–1326, https://doi.org/10.1175/1520-0469(2000)057<1311:POTMEA>2.0.CO;2, 2000.

Mulcahy, J. P., Walters, D. N., Bellouin, N., and Milton, S. F.: Impacts of Increasing the Aerosol Complexity in the Met Office Global Numerical Weather Prediction Model, Atmospheric Chemistry and Physics, 14, 4749–4778, https://doi.org/10.5194/acp-14-4749-2014, 2014.

Mulcahy, J. P., Jones, C., Sellar, A., Johnson, B., Boutle, I. A., Jones, A., Andrews, T., Rumbold, S. T., Mollard, J., Bellouin, N., Johnson, C. E., Williams, K. D., Grosvenor, D. P., and McCoy, D. T.: Improved Aerosol Processes and Effective Radiative Forcing in HadGEM3 and UKESM1, Journal of Advances in Modeling Earth Systems, 10, 2786–2805, https://doi.org/10.1029/2018MS001464, 2018.

Nakajima, T. and King, M. D.: Determination of the Optical Thickness and Effective Particle Radius of Clouds from Reflected Solar Radiation Measurements. Part I: Theory, Journal of the Atmospheric Sciences, 47, 1878–1893, https://doi.org/10.1175/1520-0469(1990)047<1878:DOTOTA>2.0.CO;2, 1990.

Nenes, A., Ghan, S., Abdul-Razzak, H., Chuang, P. Y., and Seinfeld, J. H.: Kinetic Limitations on Cloud Droplet Formation and Impact on Cloud Albedo, Tellus B: Chemical and Physical Meteorology, 53, 133–149, https://doi.org/10.1034/j.1600-0889.2001.d01-12.x, 2001.

Palmer, T. N., Doblas-Reyes, F. J., Weisheimer, A., and Rodwell, M. J.: Toward Seamless Prediction: Calibration of Climate Change Projections Using Seasonal Forecasts, Bulletin of the American Meteorological Society, 89, 459–470, https://doi.org/10.1175/BAMS-89-4-459, 2008.

Penner, J. E., Quaas, J., Storelvmo, T., Takemura, T., Boucher, O., Guo, H., Kirkeva, A., and Seland, O.: Model Intercomparison of Indirect Aerosol Effects, Atmos. Chem. Phys., 2006.

Petters, M. D. and Kreidenweis, S. M.: A single parameter representation of hygroscopic growth and cloud condensation nucleus activity, Atmospheric Chemistry and Physics, 2007.

Petty, G. W.: A First Course in Atmospheric Radiation, Sundog Publ, 2. ed edn., ISBN 978-0-9729033-1-8, 2006.

Pincus, R. and Baker, M. B.: Effect of Precipitation on the Albedo Susceptibility of Clouds in the Marine Boundary Layer, Nature, 372, 250–252, https://doi.org/10.1038/372250a0, 1994.

Platnick, S., King, M., and Hubanks, P.: MODIS (Aqua) Atmosphere L3 Monthly Product, NASA MODIS Adaptive Processing System, Goddard Space Flight Center, https://doi.org/10.5067/MODIS/MYD08_M3.061, 2017a.

Platnick, S., King, M., and Hubanks, P.: MODIS (Terra) Atmosphere L3 Monthly Product, NASA MODIS Adaptive Processing System, Goddard Space Flight Center, https://doi.org/10.5067/MODIS/MOD08_M3.061, 2017b.

Platnick, S., Meyer, K. G., King, M. D., Wind, G., Amarasinghe, N., Marchant, B., Arnold, G. T., Zhang, Z., Hubanks, P. A., Holz, R. E., Yang, P., Ridgway, W. L., and Riedi, J.: The MODIS Cloud Optical and Microphysical Products: Collection 6 Updates and Examples From Terra and Aqua, IEEE Transactions on Geoscience and Remote Sensing, 55, 502–525, https://doi.org/10.1109/TGRS.2016.2610522, 2017c.

Pruppacher, H. and Klett, J.: Microphysics of Clouds and Precipitation, vol. 18 of *Atmospheric and Oceanographic Sciences Library*, Springer Netherlands, Dordrecht, ISBN 978-0-7923-4211-3 978-0-306-48100-0, https://doi.org/10.1007/978-0-306-48100-0, 2010.

Qi, L., Li, Q., He, C., Wang, X., and Huang, J.: Effects of the Wegener–Bergeron–Findeisen process on global black carbon distribution, Atmospheric Chemistry and Physics, 17, 7459–7479, https://doi.org/10.5194/acp-17-7459-2017, 2017.

Quaas, J. and Gryspeerdt, E.: Aerosol-cloud interactions in liquid clouds, in: Aerosols and Climate, pp. 489–544, Elsevier, ISBN 978-0-12-819766-0, https://doi.org/10.1016/B978-0-12-819766-0.00019-5, 2022.

Quaas, J., Boucher, O., and Lohmann, U.: Constraining the Total Aerosol Indirect Effect in the LMDZ and ECHAM4 GCMs Using MODIS Satellite Data, Atmos. Chem. Phys., 2006.

Rasch, P. J. and Carslaw, K. S.: Aerosol–Climate Modeling, in: Aerosols and Climate, pp. 187–248, Elsevier, ISBN 978-0-12-819766-0, https://doi.org/10.1016/B978-0-12-819766-0.00009-2, 2022.

Reutter, P., Su, H., Trentmann, J., Simmel, M., Rose, D., Gunthe, S. S., Wernli, H., Andreae, M. O., and Poschl, U.: Aerosol- and Updraft-Limited Regimes of Cloud Droplet Formation: Influence of Particle Number, Size and Hygroscopicity on the Activation of Cloud Condensation Nuclei (CCN), Atmos. Chem. Phys., 2009.

Rothenberg, D. and Wang, C.: Metamodeling of Droplet Activation for Global Climate Models, Journal of the Atmospheric Sciences, 73, 1255–1272, https://doi.org/10.1175/JAS-D-15-0223.1, 2016.

Rémy, S., Kipling, Z., Huijnen, V., Flemming, J., Nabat, P., Michou, M., Ades, M., Engelen, R., and Peuch, V.-H.: Description and evaluation of the tropospheric aerosol scheme in the Integrated Forecasting System (IFS-AER, cycle 47R1) of ECMWF, Geoscientific Model Development, 15, 4881–4912, https://doi.org/10.5194/gmd-15-4881-2022, 2022.

Sayer, A. M., Munchak, L. A., Hsu, N. C., Levy, R. C., Bettenhausen, C., and Jeong, M.-J.: MODIS Collection 6 Aerosol Products: Comparison between Aqua's e-Deep Blue, Dark Target, and "Merged" Data Sets, and Usage Recommendations, Journal of Geophysical Research: Atmospheres, 119, https://doi.org/10.1002/2014JD022453, 2014.

Sayer, A. M., Hsu, N. C., Lee, J., Bettenhausen, C., Kim, W. V., and Smirnov, A.: Satellite Ocean Aerosol Retrieval (SOAR) Algorithm Extension to S-NPP VIIRS as Part of the "Deep Blue" Aerosol Project, Journal of Geophysical Research: Atmospheres, 123, 380–400, https://doi.org/10.1002/2017JD027412, 2018.

Seinfeld, J. H., Bretherton, C., Carslaw, K. S., Coe, H., DeMott, P. J., Dunlea, E. J., Feingold, G., Ghan, S., Guenther, A. B., Kahn, R., Kraucunas, I., Kreidenweis, S. M., Molina, M. J., Nenes, A., Penner, J. E., Prather, K. A., Ramanathan, V., Ramaswamy, V., Rasch, P. J., Ravishankara, A. R., Rosenfeld, D., Stephens, G., and Wood, R.: Improving Our Fundamental Understanding of the Role of Aerosol-cloud Interactions in the Climate System, Proceedings of the National Academy of Sciences, 113, 5781–5790, https://doi.org/10.1073/pnas.1514043113, 2016.

Sellegri, K., Simó, R., Wang, B., Alpert, P. A., Altieri, K., Burrows, S., Hopkins, F. E., Koren, I., McCoy, I. L., Ovadnevaite, J., Salter, M., and Schmale, J.: Influence of open ocean biogeochemistry on aerosol and clouds: Recent findings and perspectives, Elem Sci Anth, 12, 00 058, https://doi.org/10.1525/elementa.2023.00058, 2024.

SSEC, V.: VIIRS/NOAA20 Deep Blue Level 3 Monthly Aerosol Data, 1 Degree X1 Degree Grid, https://doi.org/10.5067/VIIRS/AERDB_M3_VIIRS_NOAA20.002, 2023a.

SSEC, V.: VIIRS/SNPP Deep Blue Level 3 Monthly Aerosol Data, 1 Degree X1 Degree Grid, https://doi.org/10.5067/VIIRS/AERDB_M3_VIIRS_SNPP.002, 2023b.

Stier, P., Feichter, J., Kinne, S., Kloster, S., Vignati, E., Wilson, J., Ganzeveld, L., Tegen, I., Werner, M., Balkanski, Y., Schulz, M., Boucher, O., Minikin, A., and Petzold, A.: The aerosol-climate model ECHAM5-HAM, Atmos. Chem. Phys., 2005.

Stier, P., Van Den Heever, S. C., Christensen, M. W., Gryspeerdt, E., Dagan, G., Saleeby, S. M., Bollasina, M., Donner, L., Emanuel, K., Ekman, A. M. L., Feingold, G., Field, P., Forster, P., Haywood, J., Kahn, R., Koren, I., Kummerow, C., L'Ecuyer, T., Lohmann, U., Ming, Y., Myhre, G., Quaas, J., Rosenfeld, D., Samset, B., Seifert, A., Stephens, G., and Tao, W.-K.: Multifaceted Aerosol Effects on Precipitation, Nature Geoscience, 17, 719–732, https://doi.org/10.1038/s41561-024-01482-6, 2024.

Sullivan, S. C., Lee, D., Oreopoulos, L., and Nenes, A.: Role of Updraft Velocity in Temporal Variability of Global Cloud Hydrometeor Number, Proceedings of the National Academy of Sciences, 113, 5791–5796, https://doi.org/10.1073/pnas.1514039113, 2016.

Szopa, S., Naik, V., Adhikary, B., Artaxo, P., Berntsen, T., W.D. Collins, S. Fuzzi, L. Gallardo, A. Kiendler-Scharr, Z. Klimont, H. Liao, N. Unger, and P. Zanis: The Earth's Energy Budget, Climate Feedbacks, and Climate Sensitivity, in: Climate Change 2021: The Physical Science Basis. Contribution of Working Group I to the Sixth Assessment Report of the Intergovernmental Panel on Climate Change, Cambridge University Press, 1 edn., ISBN 978-1-00-915789-6, https://doi.org/10.1017/9781009157896, 2023.

Tegen, I., Hollrig, P., Chin, M., Fung, I., Jacob, D., and Penner, J.: Contribution of Different Aerosol Species to the Global Aerosol Extinction Optical Thickness: Estimates from Model Results, Journal of Geophysical Research: Atmospheres, 102, 23 895–23 915, https://doi.org/10.1029/97JD01864, 1997.

Teng, S., Liu, C., Schnaiter, M., Chakrabarty, R. K., and Liu, F.: Accounting for the effects of nonideal minor structures on the optical properties of black carbon aerosols, Atmospheric Chemistry and Physics, 19, 2917–2931, https://doi.org/10.5194/acp-19-2917-2019, 2019.

Twomey, S.: The Influence of Pollution on the Shortwave Albedo of Clouds, Journal of the Atmospheric Sciences, 34, 1149–1152, https://doi.org/10.1175/1520-0469(1977)034<1149:TIOPOT>2.0.CO;2, 1977.

Twomey, S.: Aerosols, clouds and radiation, Atmospheric Environment. Part A. General Topics, 25, 2435–2442, https://doi.org/10.1016/0960-1686(91)90159-5, 1991.

Van Noije, T., Bergman, T., Le Sager, P., O'Donnell, D., Makkonen, R., Gon¸calves Ageitos, M., Döscher, R., Fladrich, U., Von Hardenberg, J., Keskinen, J.-P., Korhonen, H., Laakso, A., Myriokefalitakis, S., Ollinaho, P., Pérez García-Pando, C., Reerink, T., Schrödner, R., Wyser, K., and Yang, S.: EC-Earth3-AerChem: A Global Climate Model with Interactive Aerosols and Atmospheric Chemistry Participating in CMIP6, Geoscientific Model Development, 14, 5637–5668, https://doi.org/10.5194/gmd-14-5637-2021, 2021.

Verheggen, B., Cozic, J., Weingartner, E., Bower, K., Mertes, S., Connolly, P., Gallagher, M., Flynn, M., Choularton, T., and Baltensperger, U.: Aerosol partitioning between the interstitial and the condensed phase in mixed-phase clouds, Journal of Geophysical Research: Atmospheres, 112, 2007JD008 714, https://doi.org/10.1029/2007JD008714, 2007.

Wang, C., Luo, Z. J., Chen, X., Zeng, X., Tao, W.-K., and Huang, X.: A Physically Based Algorithm for Non-Blackbody Correction of Cloud-Top Temperature and Application to Convection Study, Journal of Applied Meteorology and Climatology, 53, 1844–1857, https://doi.org/10.1175/JAMC-D-13-0331.1, 2014a.

Wang, C., Soden, B. J., Yang, W., and Vecchi, G. A.: Compensation Between Cloud Feedback and Aerosol-Cloud Interaction in CMIP6 Models, Geophysical Research Letters, 48, e2020GL091 024, https://doi.org/10.1029/2020GL091024, 2021.

Wang, Q., Jacob, D. J., Spackman, J. R., Perring, A. E., Schwarz, J. P., Moteki, N., Marais, E. A., Ge, C., Wang, J., and Barrett, S. R. H.: Global budget and radiative forcing of black carbon aerosol: Constraints from pole-to-pole (HIPPO) observations across the Pacific, Journal of Geophysical Research: Atmospheres, 119, 195–206, https://doi.org/10.1002/2013JD020824, 2014b.

Wang, X., Gordon, H., Grosvenor, D. P., Andreae, M. O., and Carslaw, K. S.: Contribution of Regional Aerosol Nucleation to Low-Level CCN in an Amazonian Deep Convective Environment: Results from a Regionally Nested Global Model, Atmospheric Chemistry and Physics, 23, 4431–4461, https://doi.org/10.5194/acp-23-4431-2023, 2023.

West, R. E. L., Stier, P., Jones, A., Johnson, C. E., Mann, G. W., Bellouin, N., Partridge, D. G., and Kipling, Z.: The importance of vertical velocity variability for estimates of the indirect aerosol effects, Atmospheric Chemistry and Physics, 14, 6369–6393, https://doi.org/10.5194/acp-14-6369-2014, 2014.

Wielicki, B. A., Barkstrom, B. R., Harrison, E. F., Lee, R. B., Louis Smith, G., and Cooper, J. E.: Clouds and the Earth's Radiant Energy System (CERES): An Earth Observing System Experiment, Bulletin of the American Meteorological Society, 77, 853–868, https://doi.org/10.1175/1520-0477(1996)077<0853:CATERE>2.0.CO;2, 1996.

Wilkinson, J. M., Porson, A. N. F., Bornemann, F. J., Weeks, M., Field, P. R., and Lock, A. P.: Improved Microphysical Parametrization of Drizzle and Fog for Operational Forecasting Using the Met Office Unified Model, Quarterly Journal of the Royal Meteorological Society, 139, 488–500, https://doi.org/10.1002/qj.1975, 2013.

Wood, R.: Parametrization of the Effect of Drizzle upon the Droplet Effective Radius in Stratocumulus Clouds, Quarterly Journal of the Royal Meteorological Society, 126, 3309–3324, https://doi.org/10.1002/qj.49712657015, 2000.

Yu, H., Li, W., Zhang, Y., Tunved, P., Dall'Osto, M., Shen, X., Sun, J., Zhang, X., Zhang, J., and Shi, Z.: Organic coating on sulfate and soot particles during late summer in the Svalbard Archipelago, Atmospheric Chemistry and Physics, 19, 10 433–10 446, https://doi.org/10.5194/acp-19-10433-2019, 2019.